



APPLIED MECHANICS 2021

Liberec, 22nd April - 23th April

22nd international science conference for young researchers

22nd April - 23th April 2021, Liberec, Czech Republic

with online participation

Book of Full Texts

Technical University of Liberec,
Faculty of Mechanical Engineering, Department of Applied Mechanics

and

Czech Society for Mechanics



Text and facts may be copied and used freely, but credits should be given to these Proceedings.

All papers were reviewed by members of the scientific committee.

Copyright © 2021 Technical University of Liberec

First edition, 2021

ISBN

The conference took place online.



HEXAGON



Design & engineering simulation solutions

Smarter CAE, virtual manufacturing & costing

MSC Software, s.r.o.
Příkop 4
602 00 Brno
Telefon +420 545 176 106

www.mscsoftware.com



Table of contents

BIO	Biomechanics
COM	Computational Mechanics
DYN	Dynamics
EXP	Experimental Mechanics
MECH	Mechatronics
STR	Strength of Materials, Plasticity, Creep

Drátovská V., Sedláček R., Padovec Z.: The mechanical properties and fatigue prediction of new generation of devices for osteosynthesis (BIO)	1
Hajžman M., Očenášek J., Bulín R.: On the numerical simulations of pantographs and catenary interaction (DYN).....	7
Houdek V.: Interpolation of spatial rotations for multibody kinematics and dynamics (DYN)	16
Hrušková B., Sedláček R., Suchý T.: Evaluation of adhesion of injectable porous bone cement to bone (BIO).....	23
Kubášová K., Sedláček R., Vištejnová L., Stěpánková M., Klein P.: Effect of metallic plate fixation on mechanical properties of regenerated rib fractures (BIO)	32
Matušů M., Kropík B., Doubrava K., Ružička M., Řezníček J.: Influence of temperature increase on Young modulus of elasticity of CFRP (EXP)	36
Rágulík J., Sivčák M.: Experimental device for application of reinforcement learning algorithms to pneumatic springs (MECH)	42
Rendl J.: On the development of the software for tilting-pad journal bearing dynamics (COM)	46
Skácelík R.: Electric power distribution systems (STR)	50
Vltavský M., Sedláček R., Suchý T.: An analysis of the mechanical properties of porous ceramic foams for bone substitutes during accelerated degradation (BIO)	54

THE MECHANICAL PROPERTIES AND FATIGUE PREDICTION OF NEW GENERATION OF DEVICES FOR OSTEOSYNTHESIS

Veronika Drátovská¹, Radek Sedláček², Zdeněk Padovec³

Abstract: The aim of this work is to predict the fatigue life of metallic bone plates using SIMULIA fe-safe software and compare predicted results with measured data from experiments. Two materials commonly used for surgical implants were considered: stainless steel for implants 1.4441 (ASTM F138) and titanium alloy Ti6Al4V ELI (ASTM F136). Four-point bending fatigue test was carried out to obtain material parameters of both materials. Then the fatigue analysis based on FEA results from Abaqus was performed using the obtained material parameters. The results of the fe-safe fatigue analysis were verified by comparing them with data collected from experiments.

1. Introduction

The bone plates are in their application in human body subject to relatively high stress, that may lead to exceeding the ultimate strength of the material or more likely to the fatigue failure [1]. Failure of the bone plate may cause an additional injury and further complications for the patient and leads to excessive costs related to the reoperation [2]. Therefore, every new product needs to be tested to examine its fatigue endurance. However, fatigue experiments are quite expensive and time consuming and in the development process of new product there are usually several prototypes with different geometry, which needs to be tested to compare their fatigue properties. So, it would be interesting and useful to investigate, if there is a possibility to reliably predict the fatigue life of the bone plates.

In this paper we focused on the fatigue prediction performed by SIMULIA fe-safe software. The four-point bending fatigue test was carried out to obtain material properties for the fatigue analysis. Also, two generations of bone plates for proximal humerus fractures were tested, so we could compare the experimentally measured data with the fe-safe fatigue analysis results.

2. Methods and materials

Methodology of the four-point bending test was based on ASTM F382 standard [3], which describes static and cyclic testing of metallic bone plates. First, the static four-point bending test was performed to determine suitable loading levels for the fatigue four-point

¹ Bc. Veronika Drátovská; Czech Technical University in Prague, Faculty of Mechanical Engineering, Department of Mechanics, Biomechanics and Mechatronics, Technická 4, 160 00 Praha 6, Czech Republic, veronika.dratovska@fs.cvut.cz

² Ing. Radek Sedláček, Ph.D.; Czech Technical University in Prague, Faculty of Mechanical Engineering, Department of Mechanics, Biomechanics and Mechatronics, Technická 4, 160 00 Praha 6, Czech Republic, radek.sedlacek@fs.cvut.cz

³ Ing. Zdeněk Padovec, Ph.D.; Czech Technical University in Prague, Faculty of Mechanical Engineering, Department of Mechanics, Biomechanics and Mechatronics, Technická 4, 160 00 Praha 6, Czech Republic, zdenek.padovec@fs.cvut.cz

bending test. Afterwards, the load-controlled high-cycle fatigue test on several loading levels was done. The applied force had sinusoidal course with minimum force equal to 10 % of the maximum force (R ratio equals to 0.1). During the fatigue test the specimens were cyclically loaded until they failed. For every specimen we recorded the number of cycles the specimen reached before failure on its loading level.

To obtain material properties the four-point bending fatigue test with flat specimens with rectangular cross section was performed. From the experiment we gained number of cycles before failure and force amplitudes calculated from maximum and minimum loading force. To get a S-N curve (stress amplitude versus number of cycles curve) we calculated the stress amplitudes from the force amplitudes using equation for maximum stress in bended specimen with rectangular cross section. For the calculation of stress amplitude, we used dimensions measured for every specimen before test. Basquin's model was used, represented by equation (1), to mathematically describe the S-N curve. This model was chosen because its parameters (the fatigue strength coefficient σ'_f and the fatigue strength exponent b) are used in fe-safe. Parameters of Basquin's model were computed from measured data using linear regression.

$$\sigma_a = \sigma'_f(2N)^b \quad (1)$$

The four-point bending fatigue test with two generations of bone plates for proximal humerus fractures were carried out. The collected data were used to verify the fatigue life predicted using fe-safe.

All the experiments were performed using specimens made of stainless steel for implants 1.4441 (ASTM F138) [4] and titanium alloy Ti6Al4V ELI (ASTM F136) [5]. Both materials are commonly used for orthopaedic implants.

The data evaluated from experiments were used to define material parameters in fe-safe. However, it needed some further adjustment to be applicable in fe-safe. The experiments were carried out using $R = 0.1$, but fe-safe requires material data for fully reversed cycle ($R = -1$). Therefore, it was necessary to convert measured parameters to equivalent fully reversed cycle. Walker's equation [6] was used to compute new parameters. From the experiments we did not obtain all required fatigue parameters. So, Seeger's method was used [7] for estimation of fatigue properties using ultimate tensile strength and modulus of elasticity, to fill in the remaining parameters (the strain hardening coefficient K' , the strain hardening exponent n' , the fatigue ductility coefficient ϵ'_f , and the fatigue ductility exponent c).

In fe-safe fatigue analysis based on elastic FEA (Finite Element Analysis) results was used. The static analysis to gather these results was performed in Abaqus. Models of three generations of bone plates were made and loaded in four-point bending mode in the same configuration as in the experiments. Each bone plate was in Abaqus loaded up to 1 000 N. Results of the analysis in Abaqus (in *.odb file) were used as an input to fe-safe.

After importing the FEA results to fe-safe and choosing the relevant stress dataset it is possible to define required loading scenario. The loading cycle can be defined by two numbers, which represents the highest and the lowest load during one cycle. The stress dataset is multiplied by those numbers. For example, let us consider the stresses caused by the force equal to 1 000 N, by multiplying them by 2 and 0.2 we got the stresses for loading cycle with maximum force equal to 2 000 N and minimum force equal to 200 N. So, we can compute the analysis on several loading levels.

To perform the analysis, it is necessary to choose fatigue algorithm and method of mean stress correction. Two stress-based algorithms were used: von Mises algorithm and Normal Stress algorithm. Von Mises algorithm uses signed von Mises stress as damage parameter. Normal Stress is a critical plane multi-axial algorithm, which uses the maximal principal stress. Walker's mean stress correction was used with both algorithms.

3. Results and discussion

Results obtained from the fatigue test with flat specimens including S-N curves are shown in graph below (see Figure 1). The crosses represent destructed specimens, the circles stand for specimens without destruction. Parameters of Basquin's model were calculated using only data measured for destructed specimens. Coefficient of determination for linear regression with data measured for steel was 98.70 %, for titanium 88.85 %.

Results obtained from the fatigue tests with the real bone plates are plotted in force amplitude (see Figure 2) so we can see the differences between two generations caused by their different geometry. The first-generation bone plates were thinner and narrower than the second-generation plates and had different shape of the screw holes.

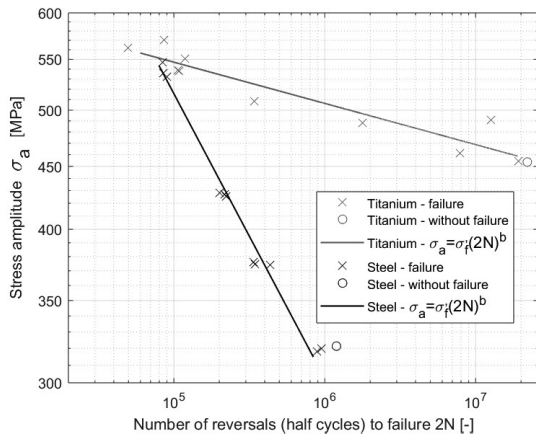


Figure 1: S-N curves for flat specimens made of steel and titanium.

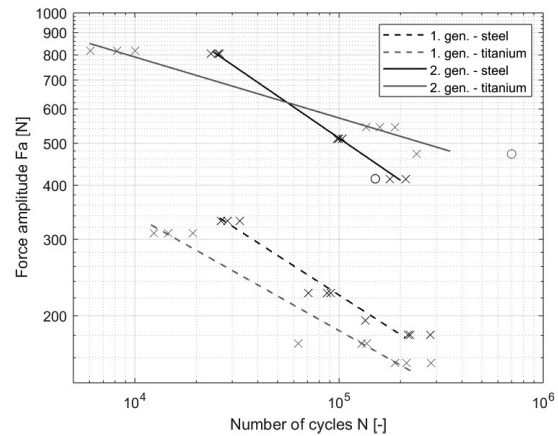


Figure 2: Measured data for the first and the second generation of steel and titanium bone plates.

All material parameters used in fe-safe are listed below (see Table 1). The table includes modulus of elasticity E , ultimate tensile strength R_m , parameter of Walker's equation γ , the parameters of Basquin's model for fully reversed cycle, and the parameters estimated using Seeger's method (as described in the previous chapter).

Table 1: Material parameters used in fe-safe analysis.

	E	R_m	γ	σ'_f	b	K'	n'	ϵ'_f	c
	[GPa]	[MPa]	[-]	[MPa]	[-]	[MPa]	[-]	[-]	[-]
Steel	173.2	1 100	0.66	9 755	-0.23	14 965	0.40	0.34	-0.58
Titanium	111.3	980	0.54	1 159	-0.03	1 220	0.05	0.35	-0.69

Output of the fe-safe analysis is number of cycles calculated for the most loaded node in the model, in other words the lowest life calculated for the whole part. It is also possible to export the results to *.odb file and display them in Abaqus as contour plot, which shows calculated fatigue life for the whole model (see Figure 3). The colour scale presents log life,

that can be converted to number of cycles using $N = 10^{\log \text{life}}$. The contour plot shows that the critical areas with the lowest fatigue life (red colour) are located around the holes. This corresponds to the areas with the highest stress.

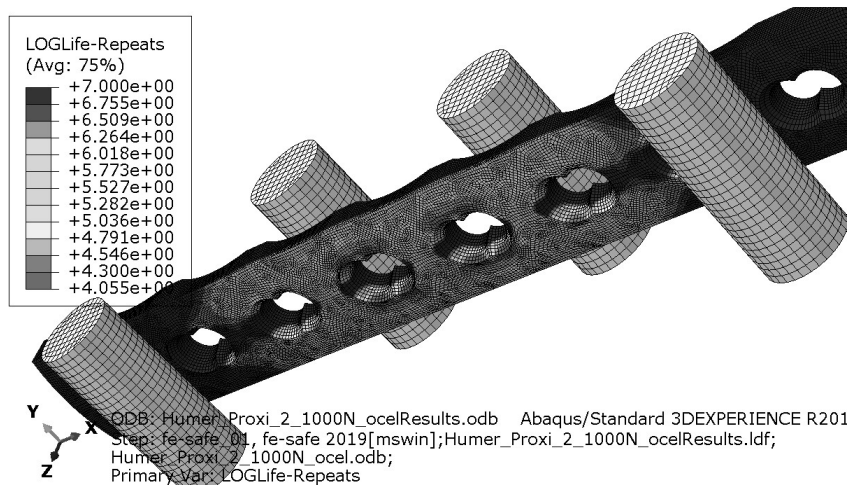


Figure 3: Results of fe-safe analysis for the second generation of steel bone plates displayed as contour plot in Abaqus.

The fe-safe analysis was run for three generations of bone plates in two material variants. Figure 4 and Figure 5 show the fe-safe prediction results compared with experiments plotted in force amplitude. The experiments are displayed as thick lines and the predictions as thinner ones, the graph contains results of both used algorithms: von Mises (VM) and Normal Stress (NS). The prediction was made for three generations, but the experiments only for the first and the second generation, because the third generation of bone plates has not been manufactured yet. Prediction for the third generation lies between the first and the second generation, this corresponds with its geometry, which is a compromise between the first and the second generation.

Figure 6 and Figure 7 display the same results plotted in stress amplitude. When the results are presented in stress amplitude the geometry of the bone plate is no longer involved and the S-N curve represents the material properties. Therefore, the predictions show the same results for all generations.

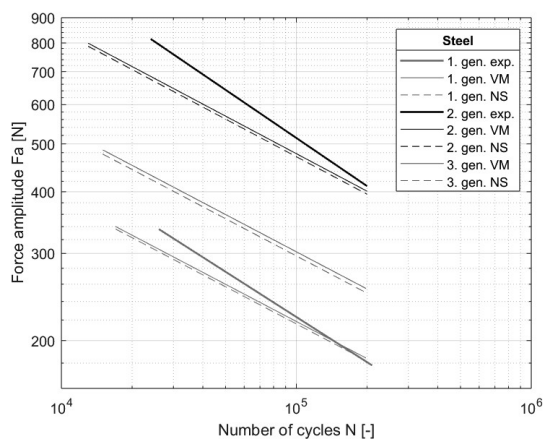


Figure 4: Comparison of experiments and fe-safe results for all generations in force amplitude – steel.

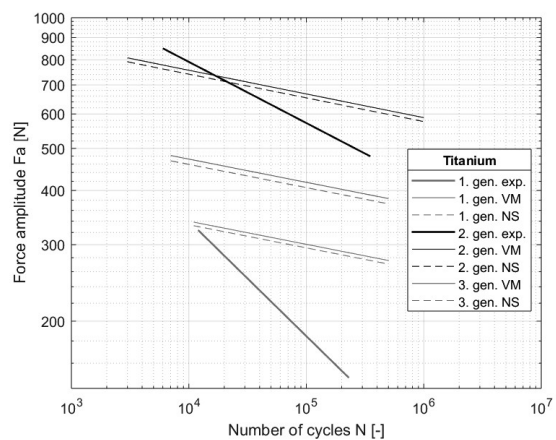


Figure 5: Comparison of experiments and fe-safe results for all generations in force amplitude – titanium.

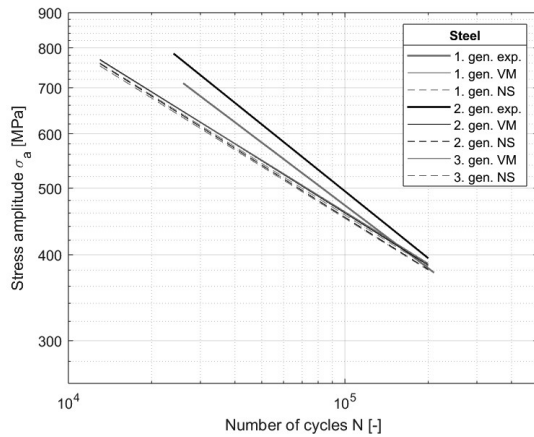


Figure 6: Comparison of experiments and fe-safe results for all generations in stress amplitude – steel.

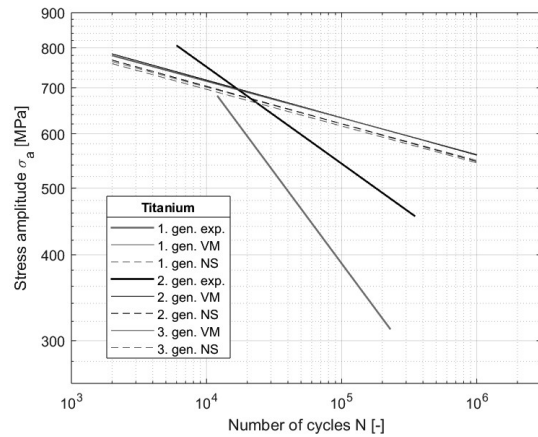


Figure 7: Comparison of experiments and fe-safe results for all generations in stress amplitude – titanium.

The fe-safe prediction for steel is quite accurate although it predicts lower fatigue life, especially for higher stress amplitudes. However, the prediction for third generation in comparison with predictions and experiments for the first and the second generation (see Figure 4) shows us, where we could expect the results of experiment with the third generation.

Results of the prediction for titanium do not really correspond with the experiments. Worse results might be caused by the input material parameters, which were for titanium computed with lower coefficient of determination. We can also see that the S-N curves from experiments with two generations of titanium bone plates (see Figure 7) differ more than the S-N curves for steel bone plates (see Figure 6), that may indicate some fluctuations in quality of used titanium material.

4. Conclusion

SIMULIA fe-safe software was used for fatigue life prediction of bone plates in two material options. The prediction was based on FEA results from Abaqus and material parameters obtained from experiments. The fe-safe analysis results were compared with the measured data from experiments. Satisfying correspondence between the prediction and the experiments for the titanium alloy was not achieved. However, the prediction for the stainless steel shows better results and could be used to estimate fatigue life of bone plates with different geometry.

5. Acknowledgments

This study was supported by the grant project awarded by the Technology Agency of the Czech Republic No. TACR TH03010418.

References

- [1] WAN, Boyang, Ali ENTEZARI, Zhongpu ZHANG et al. On fatigue failure prediction of prosthetic devices through XFEM analysis. *International Journal of Fatigue* [online]. 2021, **147** [cit. 2021-04-11]. ISSN 01421123. Available from: doi:10.1016/j.ijfatigue.2021.106160

- [2] LOGROSCINO, Giandomenico, Fabrizio DONATI, Michela SARACCO, Luciano PILLONI a Corrado PICONI. Early failure of a locked titanium plate in a proximal humeral fracture: Case report and metallurgic analysis. *Trauma Case Reports* [online]. 2018, **17**, 18-22 [cit. 2021-04-11]. ISSN 23526440. Available from: doi:10.1016/j.tr.2018.09.005
- [3] ASTM F382-17. *Standard Specification and Test Method for Metallic Bone Plates*. West Conshohocken, PA: ASTM International, 2017.
- [4] 1.4441/AISI 316L–Austenitic stainless steel for implants datasheet. *Kleinmetals* [online]. [cit. 2021-04-11]. Available from: <http://www.kleinmetals.ch/shop/Datenblatt/E/555.pdf>
- [5] TITAN Grade 23 TiAl6V4 ELI datasheet. *Kleinmetals* [online]. [cit. 2021-04-11]. Dostupné z: <http://www.kleinmetals.ch/shop/Datenblatt/E/705.pdf>
- [6] DOWLING, N. E., C. A. CALHOUN a A. ARCARI. Mean stress effects in stress-life fatigue and the Walker equation. *Fatigue & Fracture of Engineering Materials & Structures* [online]. 2009, **32**(3), 163-179 [cit. 2020-12-02]. ISSN 8756758X. Available from: doi:10.1111/j.1460-2695.2008.01322.x
- [7] Strain Based Fatigue Analysis. *Autodesk help* [online]. [cit. 2020-12-09]. Available from: <http://help.autodesk.com/view/ASMECH/2014/ENU/?guid=GUID-ECDCD9AB-BE65-43A3-9ECB-D25C38606A3E>

ON THE NUMERICAL SIMULATIONS OF PANTOGRAPHS AND CATENARY INTERACTION

Michal Hajžman¹, Jan Očenášek², Radek Bulín³

Abstract: Dynamics of the pantograph and catenary interaction is a very interesting task and it is efficient to create a dedicated software in order to have a tool for the numerical simulations of this problem. The paper deals with the description of the benchmark problem defined in the appropriate ČSN EN standard and discusses details of a particular software development.

1. Introduction

Catenary systems are mechanical systems composed of support poles and wires used in railway industry for the purpose of electrical energy transmission to a vehicle. The main components of the catenaries are shown in Fig. 1. They are interesting mechanical systems from the viewpoint of mechanics. Static problems have to be solved in the course of catenary system design. It is affected by a tension of particular wires, by the gravity force acting on the wires and mainly by the length of droppers (see Fig. 1), which are connecting contact and messenger wires and are introducing higher stiffness into the whole system. Solution of dynamic problems of the interaction of a pantograph and catenary systems is another challenge. The main features of the problem are a moving load on the contact wire caused by the pantograph and nonlinearities arising from the fact that the droppers can transmit force only in tension.

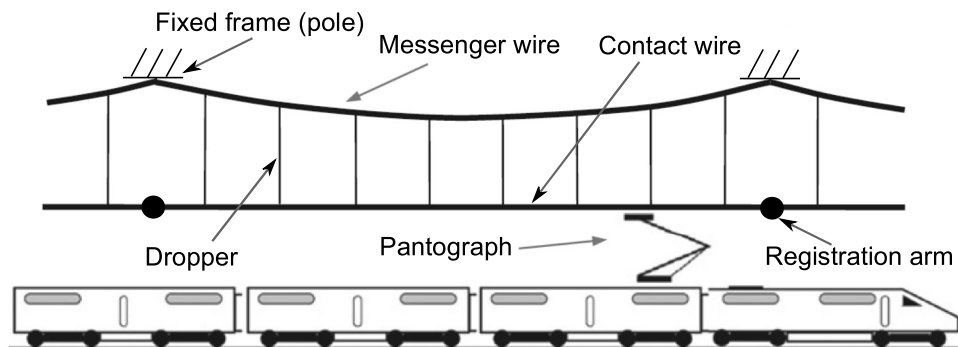


Figure 1: Scheme of a general pantograph-catenary problem with its main components.

Many researchers are interested in the problems of the pantograph and catenary interaction. The comparison of a finite element approach and a modal approach for the modelling of catenary is shown in [6]. Another approach based on semi-discretized partial differential

¹ doc. Ing. Michal Hajžman, Ph.D.; Department of Mechanics, University of West Bohemia, Univerzitní 8, 301 00 Plzeň, Czech Republic, e-mail: mhajzman@kme.zcu.cz

² Ing. Jan Očenášek, Ph.D.; New Technologies Research centre, University of West Bohemia, Univerzitní 8, 301 00 Plzeň, Czech Republic, e-mail: ocenasek@ntc.zcu.cz

³ Ing. Radek Bulín, Ph.D.; Department of Mechanics, University of West Bohemia, Univerzitní 8, 301 00 Plzeň, Czech Republic, e-mail: rbulin@kme.zcu.cz

and algebraic equations is proposed in [2] and problems with several contact wires are studied in [3]. The application of the absolute nodal coordinate formulation [8] is presented in [7]. The research interest is also dedicated to the suitable modelling of pantographs – e.g. a complex flexible multibody model [1].

The European Standard EN 50318:2002 called “Railway applications – Current collection systems – Validation of simulation of the dynamic interaction between pantograph and overhead contact line” is related to the numerical simulations of the pantograph and catenary interaction, see [4], [5]. This document defines a special benchmark problem and criteria on numerical results in order to validate developed software tools. This paper deals with the solution of the defined benchmark problem. A suitable mathematical model is introduced, several numerical results are shown and specific problems related to the solution are discussed.

2. Definition of the benchmark problem

The benchmark problem is composed of two subsystems – the pantograph and the catenary system. The problem can be viewed as a planar dynamic problem.

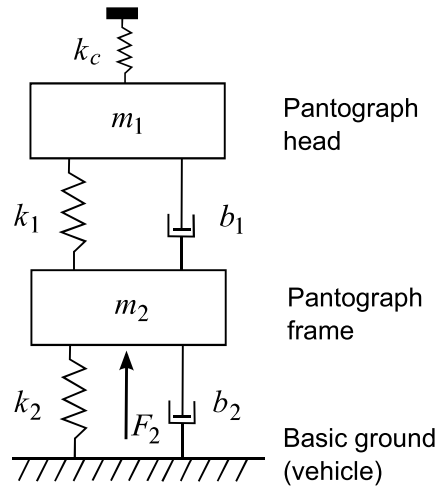


Figure 2: Pantograph model for the benchmark problem.

The motion of the pantograph is given [4], [5] by 2 degrees of freedom (see Fig. 2). A pantograph frame and a pantograph head are represented by rigid bodies with mass $m_2 = 15$ kg and $m_1 = 7.25$ kg, respectively. Elastic properties of the pantograph are given by stiffness values $k_1 = 4200$ N/m and $k_2 = 50$ N/m. Damping characteristics of the pantograph are defined by damping coefficients $b_1 = 10$ Ns/m and $b_2 = 90$ Ns/m. Uplift force $F_2 = 120$ N is acting on the pantograph frame. The contact stiffness $k_c = 5 \cdot 10^4$ N/m between the pantograph head and the contact wire is also prescribed.

The basic structure of a simple catenary system is shown in Fig. 1. The benchmark problem is prescribed [4], [5] as follows:

- The catenary system is composed of a single contact wire and a single messenger wire of prescribed density and tension force.
- The span of each field (between two poles) is 60 m.
- Number of droppers at given positions is 9 for one field. The tension stiffness of droppers is $k_{dr} = 1 \cdot 10^5$ N/m.

- Both ends of the messenger wire are fixed to the poles. Each end of the contact wire are fixed to a registration arm. The registration arm is defined as a rod of 1 m length and 1 kg weight, which has a revolute kinematic constraint to the pole.
- The overall catenary system has 10 field, i.e. the overall length is 600 m.
- The length of the droppers is not explicitly defined. It is only prescribed that the height between the contact and messenger wires at position of the poles is 1.2 m. The dropper length should be calculated in order to have the contact wire in equal height.
- The catenary system is not damped in the model.

Additional specifications of the benchmark problem are following. The testing velocities of the vehicle for the numerical simulations are 250 km/h and 300 km/h. The monitored quantity is mainly the contact force between the pantograph head and the contact wire. The numerical results are evaluated by means of statistical analysis incorporating a 20 Hz low-pass filter.

3. Mathematical model

The mathematical model of the benchmark problem should be created with respect to the definition from the previous section.

3.1. Pantograph model

The derivation of the pantograph model is clear and straightforward. The motion is given by two generalized coordinates q_1 and q_2 related to two masses m_1 and m_2 (Fig. 2)

$$\mathbf{q}_p = \begin{bmatrix} q_1 \\ q_2 \end{bmatrix}. \quad (1)$$

The pantograph model (without the effects of interaction) is of the form

$$\mathbf{M}_p \ddot{\mathbf{q}}_p + \mathbf{B}_p \dot{\mathbf{q}}_p + \mathbf{K}_p \mathbf{q}_p = \mathbf{f}_p, \quad (2)$$

where \mathbf{M}_p is the diagonal mass matrix, \mathbf{B}_p is the damping matrix, \mathbf{K}_p is the stiffness matrix and \mathbf{f}_p is the force vector containing the uplift force F_2 .

3.2. Catenary model

The mathematical model of the messenger and the contact wires can be based on several theories. The approach used in this paper applies the discretization of the wire by the planar beam finite elements with two nodes [9]. Only two degrees of freedom (vertical displacement and corresponding rotation) in each node were considered in order to minimize the size of the computational model. Thus each finite element has four generalized coordinates

$$\mathbf{q}_w^{(e)} = \begin{bmatrix} q_1^{(e)} \\ q_2^{(e)} \\ q_3^{(e)} \\ q_4^{(e)} \end{bmatrix} \quad (3)$$

and its equation of motion can be written as

$$\mathbf{M}_w^{(e)} \ddot{\mathbf{q}}_w^{(e)} + \mathbf{K}_w^{(e)} \mathbf{q}_w^{(e)} = \mathbf{f}_w^{(e)}, \quad (4)$$

where $\mathbf{M}_w^{(e)}$ is a 4×4 finite element mass matrix, $\mathbf{K}_w^{(e)}$ is the finite element stiffness matrix including the effect of geometric stiffness caused by the prescribed wire tension and $\mathbf{f}_w^{(e)}$ is the element generalized force vector describing the effect of the gravity force.

The mathematical model of the whole catenary system is finally represented as

$$\begin{bmatrix} \mathbf{M}_{cw} & \mathbf{0} \\ \mathbf{0} & \mathbf{M}_{mw} \end{bmatrix} \begin{bmatrix} \ddot{\mathbf{q}}_{cw} \\ \ddot{\mathbf{q}}_{mw} \end{bmatrix} + \begin{bmatrix} \mathbf{K}_{cw} & \mathbf{0} \\ \mathbf{0} & \mathbf{K}_{mw} \end{bmatrix} \begin{bmatrix} \mathbf{q}_{cw} \\ \mathbf{q}_{mw} \end{bmatrix} = \begin{bmatrix} \mathbf{f}_{cw} \\ \mathbf{f}_{mw} \end{bmatrix} + \mathbf{f}_{dr}(\mathbf{q}_{cw}, \mathbf{q}_{mw}), \quad (5)$$

where cw subscript indicates to the contact wire and mw subscript marks to the messenger wire, mass and stiffness matrices and vector of gravity load are created by means of model (4). The internal dropper forces are defined by vector $\mathbf{f}_{dr}(\mathbf{q}_{cw}, \mathbf{q}_{mw})$, which is nonlinear due to the “only-tension” behaviour and depends only on the stiffness of droppers and the droppers actual deformation. The forces are acting between defined nodes of the finite element mesh of the contact and messenger wire. Moreover proper boundary conditions and effects of the registration arms, with respect to the benchmark definition, are applied to the wires.

3.3. Overall model including contact forces

The whole model of the pantograph-catenary system is assembled from previously described models of the subsystems (2), (5) and it is given as

$$\begin{aligned} & \begin{bmatrix} \mathbf{M}_p & \mathbf{0} & \mathbf{0} \\ \mathbf{0} & \mathbf{M}_{cw} & \mathbf{0} \\ \mathbf{0} & \mathbf{0} & \mathbf{M}_{mw} \end{bmatrix} \begin{bmatrix} \ddot{\mathbf{q}}_p \\ \ddot{\mathbf{q}}_{cw} \\ \ddot{\mathbf{q}}_{mw} \end{bmatrix} + \begin{bmatrix} \mathbf{B}_p & \mathbf{0} & \mathbf{0} \\ \mathbf{0} & \mathbf{0} & \mathbf{0} \\ \mathbf{0} & \mathbf{0} & \mathbf{0} \end{bmatrix} \begin{bmatrix} \dot{\mathbf{q}}_p \\ \dot{\mathbf{q}}_{cw} \\ \dot{\mathbf{q}}_{mw} \end{bmatrix} + \\ & + \begin{bmatrix} \mathbf{K}_p & \mathbf{0} & \mathbf{0} \\ \mathbf{0} & \mathbf{K}_{cw} & \mathbf{0} \\ \mathbf{0} & \mathbf{0} & \mathbf{K}_{mw} \end{bmatrix} \begin{bmatrix} \mathbf{q}_p \\ \mathbf{q}_{cw} \\ \mathbf{q}_{mw} \end{bmatrix} = \begin{bmatrix} \mathbf{f}_p \\ \mathbf{0} \\ \mathbf{0} \end{bmatrix} + \begin{bmatrix} \mathbf{0} \\ \mathbf{f}_{cw} \\ \mathbf{f}_{mw} \end{bmatrix} + \\ & + \begin{bmatrix} \mathbf{0} \\ \mathbf{f}_{dr}^{(cw)}(\mathbf{q}_{cw}, \mathbf{q}_{mw}) \\ \mathbf{f}_{dr}^{(mw)}(\mathbf{q}_{cw}, \mathbf{q}_{mw}) \end{bmatrix} + \begin{bmatrix} \mathbf{f}_c^{(p)}(\mathbf{q}_p, \mathbf{q}_{cw}) \\ \mathbf{f}_c^{(cw)}(\mathbf{q}_p, \mathbf{q}_{cw}) \\ \mathbf{0} \end{bmatrix}. \end{aligned} \quad (6)$$

All matrices and vectors were described in the previous sections except the effects of the interaction between the pantograph head and the contact wire. The contact force is distributed at proper positions within vectors $\mathbf{f}_c^{(p)}$ and $\mathbf{f}_c^{(cw)}$ and its value is dependent on the generalized coordinate vectors \mathbf{q}_p and \mathbf{q}_{cw} and on the contact stiffness. The energy dissipation in the contact is not considered according to the benchmark definition.

4. Numerical solution of the problem

An in-house software tool DynPAC based on the introduced mathematical model was developed using the MATLAB system. The numerical integration of the system (6) of ordinary differential equations (ODE) has to be used because of the nonlinear character of the equations of motion. Therefore model (6) was rewritten into the ODE system of the first order to take advantage of the standard MATLAB options.

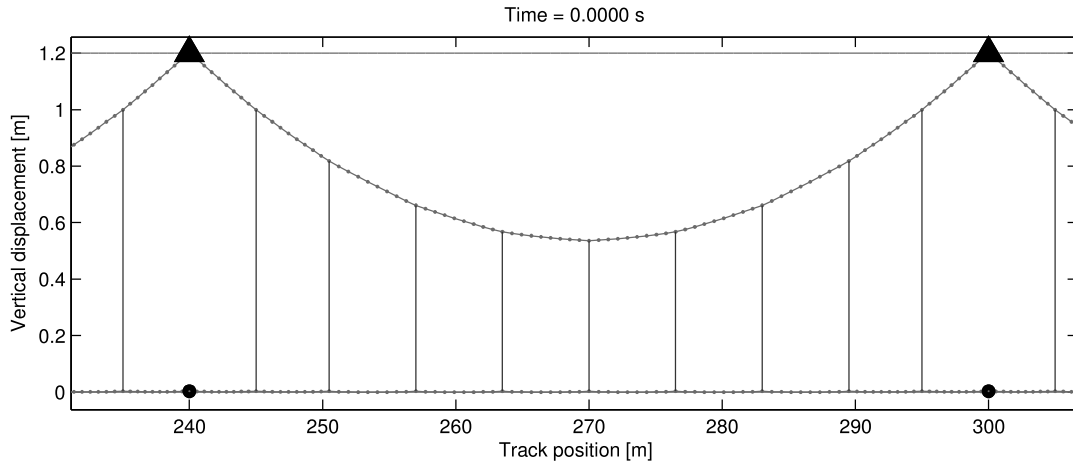


Figure 3: Illustration of the catenary system visualisation.

The initial task is to calculate the length of particular droppers for one field in order to fulfil the definition of the benchmark problem and to calculate static equilibrium for the definition of initial conditions. The static equilibrium state after the initial task is shown in Fig. 3. The equations of motion should be then numerically solved by means of standard ODE solvers of MATLAB. Several possibilities were tested and considering the numerical properties of the problem the best solvers for this task are `ode15s` (a multistep variable order solver based on the numerical differentiation formulas for stiff problems) and `ode23tb` (an implementation of TR-BDF2, an implicit Runge-Kutta formula with a first stage that is a trapezoidal rule step and a second stage that is a backward differentiation formula of order two, also for stiff problems). The in-house implementation of the Newmark method was further created as another option in order to have the alternative fixed step solver for less time consuming numerical simulations.

The illustration of calculated results are shown in Figs 4 to 10. The motion of the pantograph bodies is presented in Figs 4 and 5 for train velocity 250 km/h and 300 km/h, respectively. The main variable, which is evaluated from the numerical simulations, is the contact force between the pantograph head and the contact wire. Its time history is shown in Figs 6 and 8 for train velocity 250 km/h and 300 km/h, respectively. According to the standard [4], [5] the signal

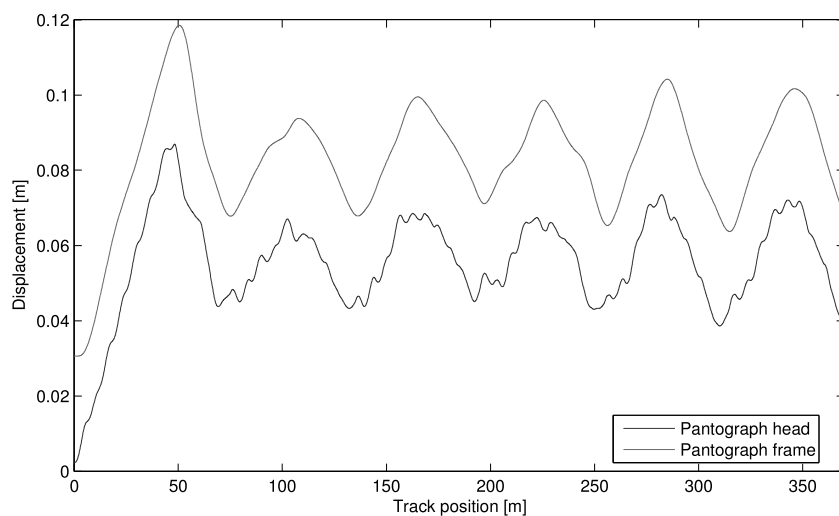


Figure 4: Time history of the pantograph displacements for 250 km/h.

should be filtered by 20 Hz low-pass filter. The filtered contact force is depicted by the red color (see Figs 6 to 9). The details of the force time history at the analytical segment (serving for the final statistical evaluation) are shown in Figs 7 and 9 for train velocity 250 km/h and 300 km/h, respectively. The most important comparison from the viewpoint of the software tool evaluation is the comparison of chosen calculated values to limits given by the EN standard (see Tab. 1 for train velocity 250 km/h).

<i>Variable</i>	<i>Simulation</i>	<i>Standard</i>
mean(F_c) [N]	116.12	110 - 120
std(F_c) [N]	28.98	26 - 31
Statistical maximum F_c [N]	203.05	190 - 210
Statistical minimum F_c [N]	29.18	20 - 40
Maximum F_c [N]	190.69	175 - 210
Minimum F_c [N]	50.18	50 - 75
Maximum reg. arm displacement [mm]	54/48/51	48 - 55

Table 1: Results of the benchmark simulation for 250 km/h.

The calculated contact force values shown in Tab. 1 should be evaluated for the analytical segment only (5th and 6th fields, i.e. on the 240 m to 360 m of the track length). The limits given in the EN standard are based on result sets obtained by certain verified numerical methods and software codes [4], [5]. As the exact form of the filter type (except the 20 Hz low-pass value) is not specified, the user of the standard has several possibilities which can have strong effect on the final filtered results.

Except the contact force the registration arm displacements at analytical segment are further important values. The calculated time history of these displacements are shown in Fig. 10 for 250 km/h.

5. Conclusion

The planar benchmark problem defined in the European standard [5], [4] was described in this paper. The purpose of the benchmark problem is to have a tool for the verification of the pantograph and catenary numerical simulations. The suitable mathematical models of the

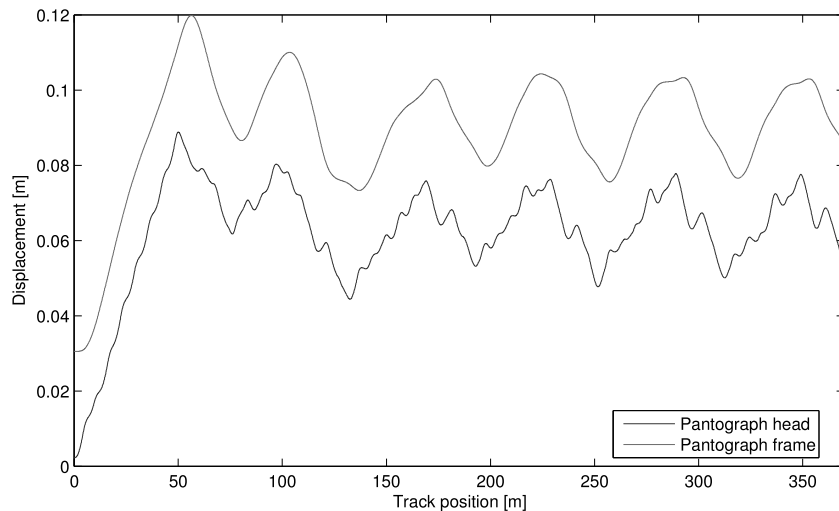


Figure 5: Time history of the pantograph displacements for 300 km/h.

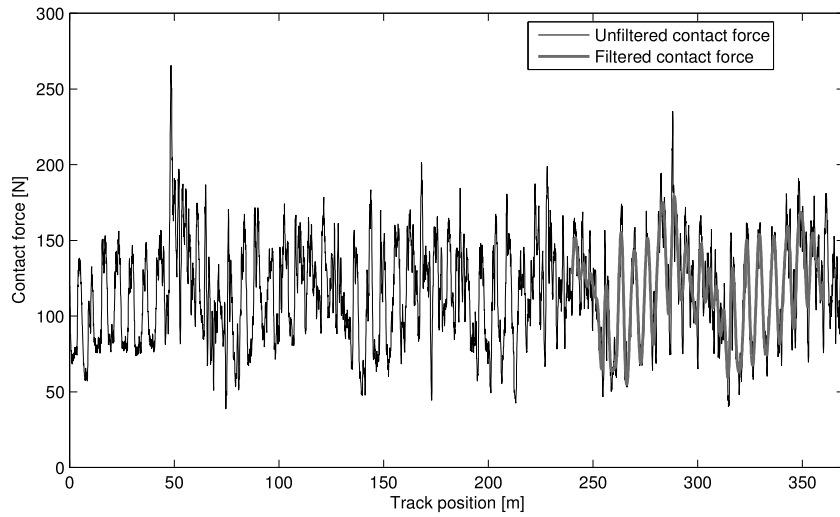


Figure 6: Time history of the contact force for 250 km/h.

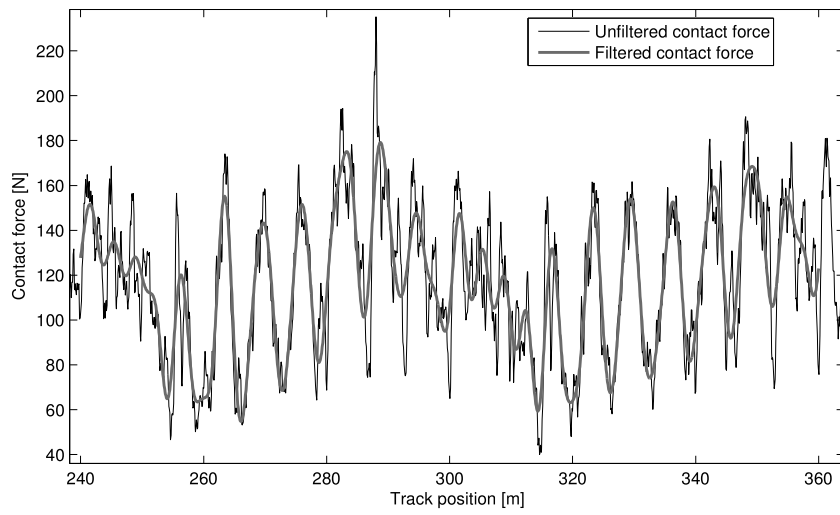


Figure 7: Time history of the contact force for 250 km/h — detail.

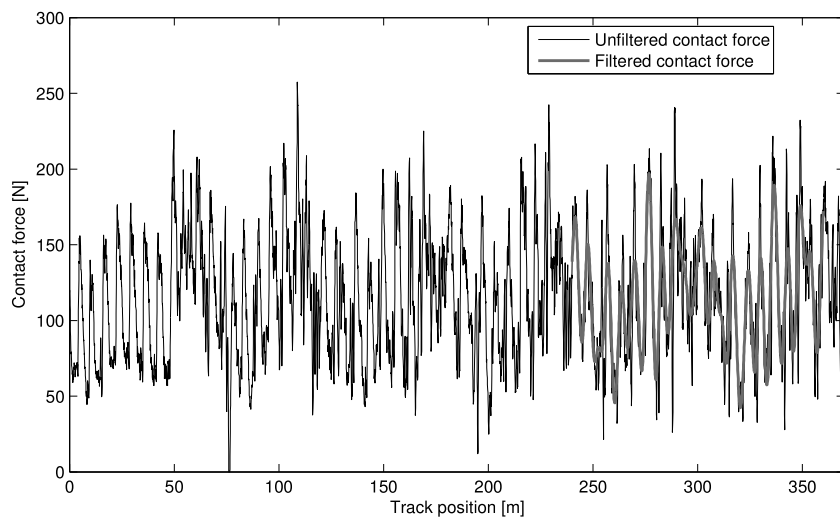


Figure 8: Time history of the contact force for 300 km/h.

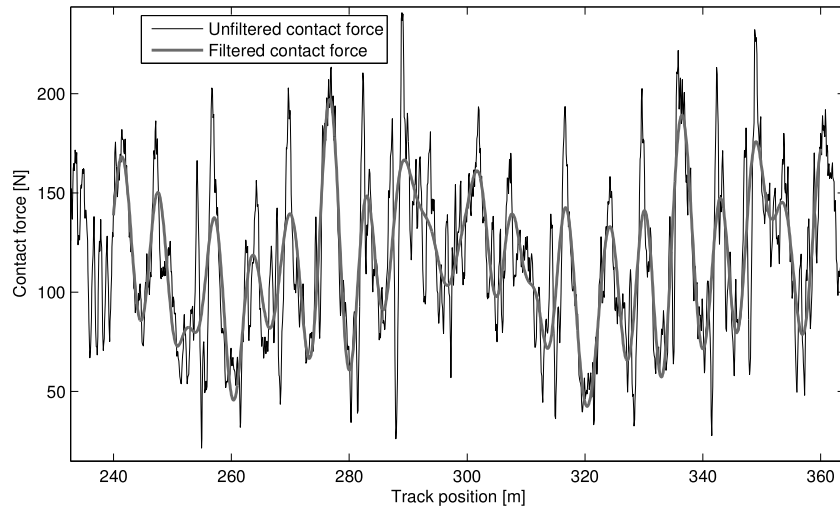


Figure 9: Time history of the contact force for 300 km/h — detail.

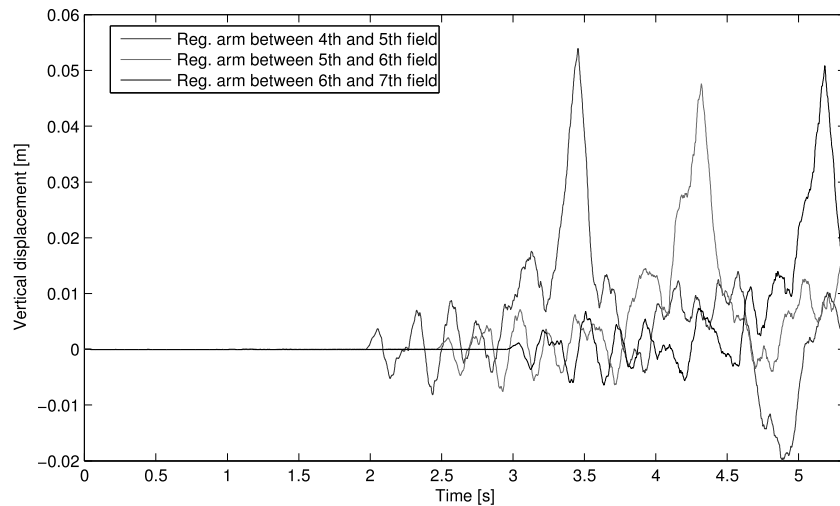


Figure 10: Time history of the registration arm displacements for 250 km/h.

pantograph and catenary system were introduced. The pantograph was modelled as the 2 DOFs lumped parameter system. The catenary model was based on the two-nodes beam finite element with 2 DOFs in each node with respect to the reduction of the size of the overall model. The droppers between contact and messenger wires were modelled by nonlinear force elements. The interaction between the pantograph head and the contact wire is represented by the moving nonlinear force. The illustrative calculated results of the numerical simulations for two train velocities are shown in the paper. The correspondence of the results with the prescribed limits defined by the EN standard is demonstrated.

The work was supported from European Regional Development Fund-Project "Research and Development of Intelligent Components of Advanced Technologies for the Pilsen Metropolitan Area (InteCom)" (No. CZ. 02.1.01/0.0/0.0/17_048/0007267).

References

- [1] Ambrósio J., Rauter F., Pombo J., Pereira M.: A flexible multibody pantograph model for the analysis of the catenary-pantograph contact problem, Proc. of ECCOMAS Thematic Conference on Multibody Dynamics 2009, Warsaw, ECCOMAS, 2009, CD-ROM
- [2] Arnold M., Simeon B.: Pantograph and Catenary Dynamics: A Benchmark Problem and Its Numerical Solution, Applied Numerical Mathematics, Vol. 34, 2000, pp. 345-362
- [3] Benet J., Alberto A., Arias E., Rojo T.: A Mathematical Model of the Pantograph-Catenary Dynamic Interaction with Several Contact Wires, IAENG International Journal of Applied Mathematics 37:2, 2007, IJAM_37_2_10
- [4] ČSN EN 50318 Drn zazen – Systmy odbru proudu – Oovovn simulace dynamick interakce mezi pantografovnm sbraem a nadzemnm trolejovnm vedenm. esk technick norma, esk normalizan institut, 2003
- [5] EN 50318:2002 Railway applications – Current collection systems – Validation of simulation of the dynamic interaction between pantograph and overhead contact line. International technical standard, 2002
- [6] Kia S.H., Bartolini F., Mpanda-Mabwe A., Ceschi R.: Pantograph-Catenary Interaction Model Comparison, Proc. of IECON 2010 - 36th Annual Conference on IEEE Industrial Electronics Society, Glendale, IEEE, 2010, pp. 1584-1589
- [7] Seo J.H. , Kim S.W. , Jung I.H. , Park T.W. , Mok J.Y. , Kim Y.G., Chai, J.B.: Dynamic analysis of a pantograph-catenary system using absolute nodal coordinates, Vehicle System Dynamics, Vol. 44, 2006, pp. 615-630
- [8] Shabana A.A.: Dynamics of Multibody Systems. 3rd ed. Cambridge, New York, 2005
- [9] Przemieniecki J.S.: Theory of Matrix Structural Analysis. Dover, New York, 1985

INTERPOLATION OF SPATIAL ROTATIONS FOR MULTIBODY KINEMATICS AND DYNAMICS

Václav Houdek¹, Michal Hajžman², Olivier Verlinden³

Abstract: This paper deals with the interpolation of spatial rotations of a body in space for the purpose of multi-body kinematics and dynamics. The most important methods of spatial rotation parametrization are summarized at first (e.g. Euler angles, Bryant angles, Euler parameters, quaternion representation). The main contribution of this paper is the usage of look up tables of a body configuration in 3D for the purpose of rotation interpolation with the advantage of computational costs reduction. Particularly, the spline interpolation is introduced and its special form of B-spline is explained. Final part of the paper deals with quaternion B-spline interpolation, whose advantage is the C^n continuity of interpolated data. In this paper C^2 continuity was achieved.

1. Introduction

Parametrization of finite rotations is an essential issue in rigid body and multibody dynamics. It is related to the description of body rotation in space usable in kinematical and dynamical equations. The position of a body, its translational velocity and corresponding acceleration are usually easy to describe. However, the composition and parametrization of rotations are more demanding. The motivation of the work presented in this paper is the efficient solution of kinematics for the purpose of vehicle dynamics problems. The main idea is to pre-compute the rotation parameters of the body and then use the interpolation of rotations in the framework of more complex computational tasks. High usability of the interpolation lies especially in fast dynamic simulations during optimization processes, e.g. searching of an optimal geometry of a car suspension.

This paper is divided into two main parts. Firstly spatial rotation parametrization is briefly summarized. The second part of the paper deals with the rotation interpolation. The rotations are expressed by quaternions and interpolation is based on B-spline curves.

2. Spatial rotation parametrization

There are several common ways how to describe a spatial orientation of a body, which has six degrees of freedom considering completely free motion. Thus three degrees of freedom belong to the rotation. The natural way how to parametrize the spatial rotations is to use three suitable angles.

The Euler angles go from global frame to local frame by three successive rotations about Z, X and Z local axes by angles classically denoted respectively by ϕ , θ and ψ . The

¹ Ing. Václav Houdek; University of West Bohemia, Faculty of Applied Sciences; Univerzita 8, 301 00 Plzeň, Czech Republic, vaclavh@kme.zcu.cz

² doc. Ing. Michal Hajžman, Ph.D.; University of West Bohemia, Faculty of Applied Sciences; Univerzita 8, 301 00 Plzeň, Czech Republic, mhajzman@kme.zcu.cz

³ prof. Olivier Verlinden; University of Mons, Faculty of Engineering; Rue de Houdain 9, 7000 Mons, Belgium, e-mail: olivier.verlinden@umons.ac.be

corresponding rotation matrix is obtained in the form

$$\begin{aligned} \mathbf{R}_{0,i} &= \begin{pmatrix} \cos \phi & -\sin \phi & 0 \\ \sin \phi & \cos \phi & 0 \\ 0 & 0 & 1 \end{pmatrix} \cdot \begin{pmatrix} 1 & 0 & 0 \\ 0 & \cos \theta & -\sin \theta \\ 0 & \sin \theta & \cos \theta \end{pmatrix} \cdot \begin{pmatrix} \cos \psi & -\sin \psi & 0 \\ \sin \psi & \cos \psi & 0 \\ 0 & 0 & 1 \end{pmatrix} = \\ &= \begin{pmatrix} \cos \phi \cos \psi - \sin \phi \cos \theta \sin \psi & -\cos \phi \sin \psi - \sin \phi \cos \theta \cos \psi & \sin \phi \sin \theta \\ \sin \phi \cos \psi + \cos \phi \cos \theta \sin \psi & -\sin \phi \sin \psi + \cos \phi \cos \theta \cos \psi & -\cos \phi \sin \theta \\ \sin \theta \sin \psi & \sin \theta \cos \psi & \cos \theta \end{pmatrix} \end{aligned} \quad (1)$$

The major drawback of the Euler angles is a singularity when $\theta = 0$ or π , in which case both intermediate rotation axes about Z become collinear: the rotation is then reduced to a single rotation ($\phi \pm \psi$) about Z.

The Bryant angles go from global frame to local frame by three successive rotations about Z, Y and X local axes by angles classically denoted respectively by ψ , θ and ϕ and called yaw, pitch and roll. The corresponding rotation matrix is obtained in the following way

$$\begin{aligned} \mathbf{R}_{0,i} &= \begin{pmatrix} \cos \psi & -\sin \psi & 0 \\ \sin \psi & \cos \psi & 0 \\ 0 & 0 & 1 \end{pmatrix} \cdot \begin{pmatrix} \cos \theta & 0 & \sin \theta \\ 0 & 1 & 0 \\ -\sin \theta & 0 & \cos \theta \end{pmatrix} \cdot \begin{pmatrix} 1 & 0 & 0 \\ 0 & \cos \phi & -\sin \phi \\ 0 & \sin \phi & \cos \phi \end{pmatrix} = \\ &= \begin{pmatrix} \cos \psi \cos \theta & \cos \psi \sin \theta - \cos \phi \sin \psi & \sin \phi \sin \psi + \cos \phi \cos \psi \sin \theta \\ \cos \theta \sin \psi & \cos \phi \cos \psi + \sin \phi \sin \psi \sin \theta & \cos \phi \sin \psi \sin \theta - \cos \psi \sin \phi \\ -\sin \theta & \cos \theta \sin \phi & \cos \phi \cos \theta \end{pmatrix}. \end{aligned} \quad (2)$$

Also the major drawback of the Bryant angles is a singularity when $\theta = \pm\pi/2$, in which case intermediate rotation axes about Z and X become collinear: the rotation is then reduced to a single rotation ($\phi \pm \psi$) about the Z global axis.

Another rotation parametrization is based on a different approach. Let us consider a rotation by an angle ϕ about an axis whose direction cosines are worth n_x , n_y and n_z . The corresponding rotation matrix can be written in the form

$$\mathbf{R}_{0,i} = \begin{pmatrix} 1 - 2(e_2^2 + e_3^2) & 2(e_1e_2 - e_0e_3) & 2(e_1e_3 + e_0e_2) \\ 2(e_1e_2 + e_0e_3) & 1 - 2(e_1^2 + e_3^2) & 2(e_2e_3 + e_0e_1) \\ 2(e_1e_3 - e_0e_2) & 2(e_2e_3 + e_0e_1) & 1 - 2(e_1^2 + e_2^2) \end{pmatrix}, \quad (3)$$

where e_0 , e_1 , e_2 and e_3 are called Euler parameters and are defined by

$$e_0 = \cos \frac{\phi}{2}, \quad e_1 = n_x \cos \frac{\phi}{2}, \quad e_2 = n_y \cos \frac{\phi}{2}, \quad e_3 = n_z \cos \frac{\phi}{2}.$$

There are four parameters instead of three but they are linked by the constraint

$$e_0^2 + e_1^2 + e_2^2 + e_3^2 = 1.$$

The four Euler parameters are often used with Cartesian coordinates because they do not give rise to any singularity and lead to simple expressions of rotation matrices, velocities and accelerations avoiding the computation of sines and cosines. The presence of a supplementary constraint equation is not a real drawback in the context of Cartesian coordinates as there exist anyway several constraint equations for the joints.

Quaternions were firstly introduced by W. R. Hamilton in 1866 [12]. The quaternion number system extends the complex numbers. General representation of the quaternion is

$$\hat{q} = a + b\mathbf{i} + c\mathbf{j} + d\mathbf{k}, \quad (4)$$

which can be understood as four-dimensional complex number. a, b, c and d are real numbers and i, j and k are imaginary units (also known as fundamental quaternions units), which can be interpreted as unit-vectors pointing along the three spatial axes.

Quaternions can be easily converted to so called axis-angle representation. A spatial rotation around a fixed point of θ radians about a unit axis (X, Y, Z) that denotes the Euler axis is given by the quaternion (C, XS, YS, ZS) , where $C = \cos(\theta/2)$ and $S = \sin(\theta/2)$.

3. Spline interpolation and B-spline

Generally, *spline interpolation* is a form of interpolation where the interpolant is a special type of piecewise polynomial called a spline. That is advantageous, instead of fitting a single, high-degree polynomial to all of the values at once. Spline interpolation fits low-degree polynomials to small subsets of the values. For example, fitting nine cubic polynomials between each of the pairs of ten points, instead of fitting a single degree-ten polynomial to all of them. Spline interpolation is often preferred over polynomial interpolation because the interpolation error can be made small even when using low degree polynomials for the spline [9]. Spline interpolation also avoids the problem of Runge's phenomenon, in which oscillation can occur between points when interpolating using high degree polynomials.

Generally, *B-spline* or basis spline is a spline function that has minimal support with respect to a given degree, smoothness, and domain partition. Any spline function of given degree can be expressed as a linear combination of B-splines of that degree. B-splines can be used for curve-fitting and numerical differentiation of experimental data. Its formula is recurrent [10].

In computer-aided design and computer graphics, spline functions are constructed as linear combinations of B-splines with a set of control points.

The base functions $B_i^k(t)$'s are defined by the following recurrence relation [11]:

$$B_i^1(t) = \begin{cases} 1 & t_i \leq t \leq t_{i+1} \\ 0 & \text{otherwise} \end{cases} \quad (5)$$

and

$$B_i^k(t) = \frac{t - t_i}{t_{i+k-1} - t_i} B_i^{k-1}(t) + \frac{t_{i+k} - t}{t_{i+k} - t_{i+1}} B_{i+1}^{k-1}(t). \quad (6)$$

4. Quaternion interpolation

Unit quaternions play an important role not only in multi-body dynamics but also in computer graphics and animation as a computationally usable tool for controlling rotation for both object, models and virtual cameras [1, 2]. Advantage of the unit quaternions is a lack of singularities such as gimbal lock. Furthermore, unit quaternion are computationally more efficient than the 3×3 matrix representation of 3D rotation. Thus, the design of various quaternion curves has become an active research topic in computer graphics [2, 3].

B-spline Quaternion curve

Let us start with simple B-spline curve $P(t)$ of order k based on $n + 1$ control points $\{p_i\}$, where $i = 0, \dots, n$, this curve is defined as

$$P(t) = \sum_{i=0}^n p_i B_i^k(t), \quad (7)$$

where $B_i^k(t)$ are the basis functions. The basis functions are C^{k-2} continuous piecewise polynomials of degree $(k-1)$. They are C^{k-2} continuous everywhere, but may not be C^{k-1} continuous at the knot sequence $\{t_i\}$. Each $B_i^k(t)$ has a non-zero support on the interval $[t_i, t_{i+k}]$, i.e., $B_i^k(t) = 0$ for $t < t_i$ or $t > t_{i+k}$ [7]. The B-spline curve can be reformulated as

$$P(t) = p_0 \tilde{B}_0^k(t) + \sum_{i=1}^n (p_i - p_{i-1}) \tilde{B}_i^k(t). \quad (8)$$

By replacing $P(t)$ to $\hat{Q}(t)$, p_i to \hat{q}_i , and the summations to the quaternion multiplications [13], the corresponding B-spline quaternion curve with a cumulative basis form is formulated as

$$\hat{Q}(t) = \hat{q}_0^{\tilde{B}_0^k(t)} \prod_{i=0}^{n+1} (\hat{q}_{i-1}^{-1} \hat{q}_i)^{\tilde{B}_i^k(t)}, \quad (9)$$

which interpolates a given sequence of data quaternions \hat{Q}_i ($i = 0, 1, \dots, n$). The control points \hat{q}_i are explained in next section and $\tilde{B}_i^k(t) \equiv \tilde{B}_i^4(t) \equiv \tilde{B}_i(t)$ which is defined as

$$\tilde{B}_i(t) = \sum_{j=i}^{n+1} B_j(t), \quad (10)$$

Control points computation

Because there are $n+1$ values of \hat{Q}_i for $n+3$ unknown control points $\hat{q}_{-1}, \hat{q}_0, \dots, \hat{q}_{n+1}$, two boundary conditions are needed. The end conditions for natural spline are

$$\hat{Q}''(0) = [0\ 0\ 0\ 0] \quad \text{and} \quad \hat{Q}''(n) = [0\ 0\ 0\ 0]. \quad (11)$$

when these two boundary conditions are applied, we obtain non-linear system of equations [7]

$$\hat{q}_{-1} = \hat{q}_0 (\hat{q}_0^{-1} \hat{q}_1)^{-1}, \quad (12)$$

$$\hat{q}_0 = \hat{Q}_0, \quad (13)$$

$$\hat{q}_{i-1} (\hat{q}_{i-1}^{-1} \hat{q}_i)^{\frac{5}{6}} (\hat{q}_i^{-1} \hat{q}_{i+1})^{\frac{1}{6}} = \hat{Q}_i, \quad \text{for } i = 1, 2, \dots, n-1, \quad (14)$$

$$\hat{q}_n = \hat{Q}_n, \quad (15)$$

$$\hat{q}_{n+1} = \hat{q}_n (\hat{q}_n^{-1} \hat{q}_{n+1}). \quad (16)$$

There is no known method to compute the exact solution, so the iterative method is proceeded to solve this system. The iterative method comes from the equation (14). The dominant term on the left hand side is $(\hat{q}_{i-1}^{-1} \hat{q}_i)^{\frac{5}{6}}$, by solving it for this term [7]

$$(\hat{q}_{i-1}^{-1} \hat{q}_i)^{\frac{5}{6}} = \hat{q}_{i-1}^{-1} \hat{Q}_i (\hat{q}_i^{-1} \hat{q}_{i+1})^{-\frac{1}{6}}, \quad (17)$$

$$\hat{q}_i^* = \hat{q}_{i-1} \left[\hat{q}_{i-1}^{-1} \hat{Q}_i (\hat{q}_i^{-1} \hat{q}_{i+1})^{-\frac{1}{6}} \right]^{\frac{6}{5}}. \quad (18)$$

For the initial guess, $\hat{q}_i = \hat{Q}_i$ is considered. However, due to the non-linearity of the problem, there are some restrictions for the input values of \hat{Q}_i 's so that the convergence of the iterative method is guaranteed. This is the topic of next subsection.

Angle error

Every rotation in a three-dimensional Euclidean space can be parametrized by two quantities: a unit vector \mathbf{e} indicating the direction of an axis of rotation, and an angle θ describing the magnitude of the rotation about the axis.

For a given input sequence of keyframe orientations \hat{Q}_i 's, let the angle distance θ_i and the axis difference ϕ_i be defined by

$$\theta_i = \left| \log(\hat{Q}_{i-1}^{-1} \hat{Q}_i) \right|, \quad (19)$$

$$\phi_i = \left| \mathbf{e}_{i-1,i} \times \mathbf{e}_{i,i+1} \right|, \quad (20)$$

where $\mathbf{e}_{i-1,i}$ and $\mathbf{e}_{i,i+1}$ are unit vectors indicating the direction of an axis of relative rotation between orientation \hat{Q}_{i-1} and \hat{Q}_i , and \hat{Q}_i and \hat{Q}_{i+1} respectively, and $'\times'$ is the cross product. Quaternion \hat{Q}_r which express relative rotation between orientation $i - 1$ and i , is obtained by

$$\hat{Q}_r = \hat{Q}_{i-1}^{-1} \hat{Q}_i = a_r + b_r \mathbf{i} + c_r \mathbf{j} + d_r \mathbf{k}. \quad (21)$$

Then the axis of relative rotation is defined as

$$\mathbf{e} = \frac{(b_r, c_r, d_r)}{\sqrt{b_r^2 + c_r^2 + d_r^2}}. \quad (22)$$

5. Example

The introduced methodology for the quaternion spline interpolation was tested on the car suspension system (see fig. 1). In this section of the paper, the results obtained by the introduced method are compared with the results by the interpolation using combination of Hermite splines and homogeneous transformation matrices.

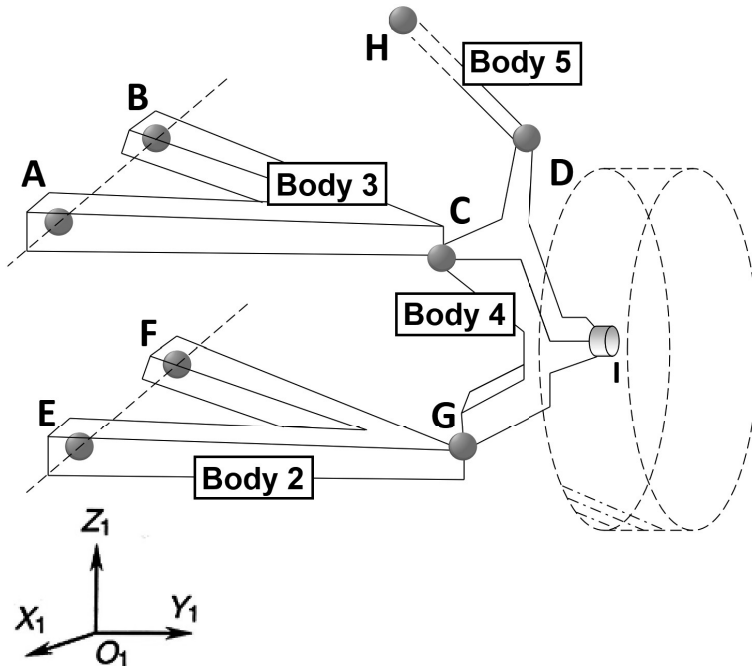


Figure 1: Scheme of a double wishbone suspension.

It is assumed that steering and spinning of the wheel (representing two DOFs) are locked. The conventional suspension then becomes a mechanism with one DOF. The driving parameter is the vertical coordinate of the wheel support (z coordinate).

In the case of rotation interpolation in 3D, the lookup table with four columns is needed. First column is driving parameter - z coordinate of the wheel support, and three other columns are angles - e.g. Euler angles, Tait-Bryan angles, Cardan angles, which are converted to quaternions. Bryant angles are used in this paper, because they come from numerical solution of the suspension kinematics, which serves as an input for the lookup table creation.

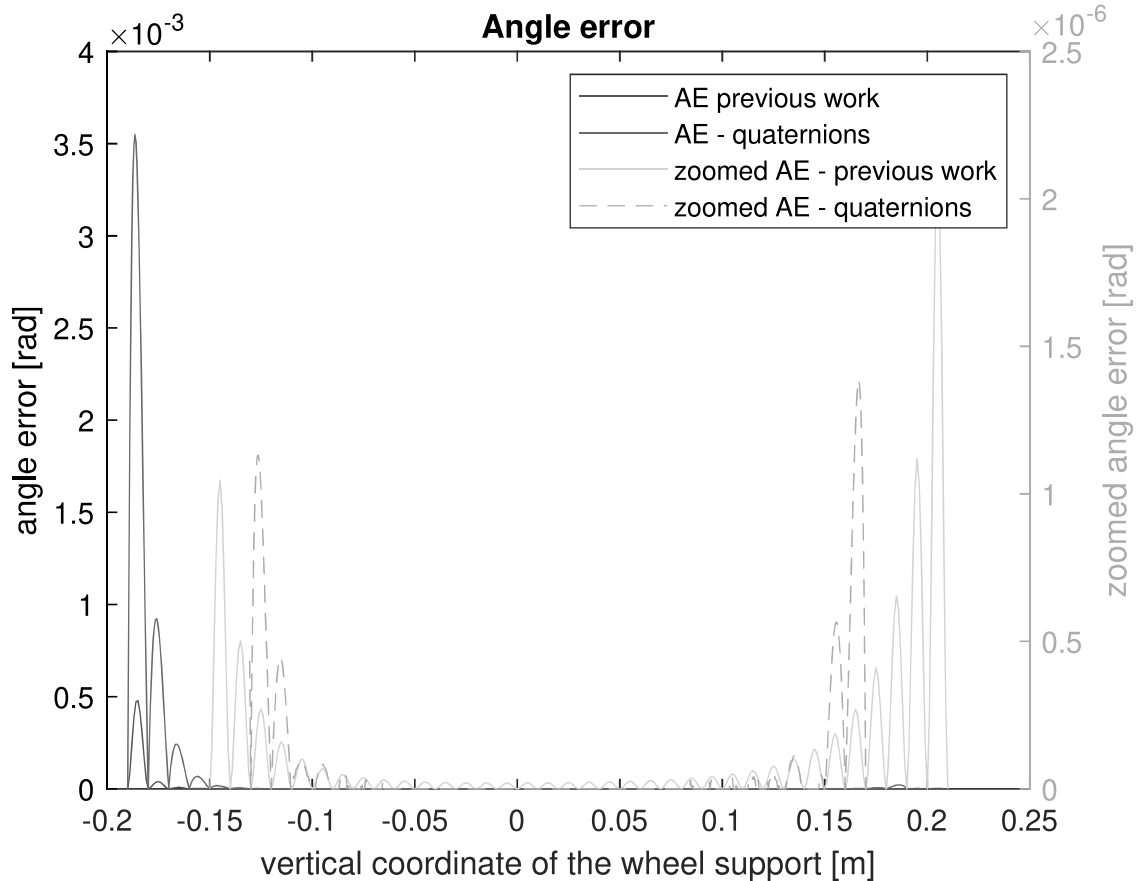


Figure 2: Results of the calculation.

Illustrative results are shown in fig. 2. There are results obtained by the proposed interpolation method (red curve) and the results obtained by interpolation based on cubic Hermite splines and transformation matrices (blue curve). The same results are depicted as dashed orange plot and green plot, but they are zoomed in order to see the details. The shortcut AE stands for the angle error.

It can be seen, from certain point the angle error of the proposed interpolation is zero, whereas the other interpolation has zero error only in control points.

6. Conclusion

The methodology introduced in this paper can be used for the pre-computation and interpolation of the rotation parameters of bodies in the framework of more complex computational

tasks. It is motivated mainly by the problems of vehicle kinematics and dynamics. The spatial rotations are parametrized by quaternions in this work. The proposed methodology was implemented in MATLAB and tested on the double wishbone suspension. The exact position and orientation (of a wheel) were compared with the calculated values obtained from the interpolation in order to verify the method.

The introduced interpolation gives at some interval better results than the other interpolation. It may be due to a decrease of angle distance or axis difference (θ_i or ϕ_i), because the closer the wheel is to the zero value of vertical coordinate of the wheel support, the smaller is the angle distance θ_i . This can be the subject of the future research and parametric study of angle distance and axis difference can be proceeded.

This research work was supported by project SGS-2019-009 of Czech Ministry of Education, Young and Sport.

References

- [1] M. Gleicher and A. Witkin. Through-the-lens camera control. *Computer Graphics*, pages 331–340, 1991.
- [2] K. Shoemake. Animating rotation with quaternion curves. *Computer Graphics*, pages 245–254, 1985.
- [3] G. M. Nielson. ν quaternion splines for the smooth interpolation of orientations. *IEEE Transactions on Visualization and Computer Graphics*, 10(2), March/April 2010.
- [4] M. Curtis. Matrix groups. *Springer-Verla*, 1972.
- [5] W.R. Hamilton. Elements of quaternions. *Chelsea Publishing Company*, 1866.
- [6] J.L. Junkins and J.D. Turner. Optimal spacecraft rotational maneuvers. *Elsevier*, 1986.
- [7] M. J. Kim, M. S. Kim, and S. Y. Shin. A c2-continuous b-spline quaternion curve interpolating a given sequence of solid orientations. *Computer Animation 95, IEEE CS Press*, 1995.
- [8] J. Gallier. The Quaternions and the Spaces S^3 , $SU(2)$, $SO(3)$, and $\mathbb{R}P^3$. *Geometric Methods and Applications [online]*. New York, NY: Springer New York, 2001.
- [9] J. H. Ahlberg, E. N. Nilson, J. L. Walsh. The theory of Splines and Their Applications. *Academic Press. New York and London*, 1967.
- [10] G. D. Knott. Interpolating Cubic Splines *Birkhuser Boston*, 2000.
- [11] C. Boor. *A Practical Guide to Splines*. Springer-Verlag, 1978.
- [12] L. C. Bruno. Math and mathematicians : the history of math discoveries around the world. *Baker, Lawrence W. Detroit, Mich.: U X L.*, 1999.
- [13] P. Gille, T. Szamuely Central simple algebras and Galois cohomology. Cambridge Studies in Advanced Mathematics. *Cambridge: Cambridge University Press*, 2006.

EVALUATION OF ADHESION OF INJECTABLE POROUS BONE CEMENT TO BONE

Barbora Hrušková¹, Radek Sedláček², Tomáš Suchý³

Abstract: The aim of this work was to perform an evaluation of the adhesion of injectable bone cements, potentially utilized as a fully resorbable alternative to the standard non-degradable cements. An experimental evaluation of the adhesion of five differently modified bone cements to bone was performed, namely the cement itself based on a copolymer of PLGA-PEG-PLGA and calcium phosphate (CPC), which was further modified with three different admixtures (antibiotics, PCL nanofibers and dopamine). Standard bone cement based on PMMA was used as a control material. The tests were performed on two types of implants made of titanium alloy Ti6Al4 ELI. The first type (type I) was an implant with plasma-sprayed hydroxyapatite coating, the second type was a 3D printed implant with a trabecular surface structure. The test implants were fixed *ex vivo* in porcine femurs for the time required for their hardening (72 hours). The methodology of the experiment was based on determining the maximum force required to break the adhesion in pull-out tests. Other evaluated parameters were the displacement at failure and the shear strength. For PMMA cement, the highest evaluated shear strength using pull-out tests was at 3.4 ± 1.6 MPa (implant type I) and the shear strength for dopamine-doped CPC was 1.3 ± 0.58 MPa (implant type I). The shear strength of CPC with dopamine was at 38% of PMMA shear strength, the value of displacement at failure was only 47% lower compared to PMMA. The results show a lower degree of adhesion of the evaluated cements, but the observed decrease in the initial healing phase may not be limiting for specific applications.

1. Introduction

Healthy bones are the basis for the proper function of the musculoskeletal system. Bones can heal themselves, but if the bone defect is too large, this natural process is not enough to completely regenerate the bone. Bone substitutes are commonly used in surgery in these cases. Bone substitutes are widely applied not only in surgery, but also in traumatology, oncology, or orthopaedics. Currently, the gold standard in the treatment of bone trauma is the bone graft, but its application brings several complications, including the risk of infection which treatment is associated with the need of reoperation. Due to these complications, there is a great need for alternative synthetic materials. The required properties of these materials are their biotolerance, biodegradability, injectability and bone-like mechanical properties. Today's commonly used material is synthetic polymer polymethylmethacrylate (PMMA), which is biotolerant and has suitable mechanical properties. However, its disadvantage is its inability to undergo natural degradation processes in the body, it is not injectable, and it heats up during its hardening, which can cause bone necrosis. Today, attention is drawn to calcium phosphate-based cements

¹ Bc. Barbora Hrušková; Czech Technical University in Prague, Faculty of Mechanical Engineering, Department of Mechanics, Biomechanics and Mechatronics; Technická 4, 160 00 Praha 6, Czech Republic, Barbora.Hruskova@fs.cvut.cz

² Ing. Radek Sedláček, PhD.; Czech Technical University in Prague; Faculty of Mechanical Engineering, Department of Mechanics, Biomechanics and Mechatronics, Technická 4, 160 00 Praha 6, Czech Republic, Radek.Sedlacek@fs.cvut.cz

³ Ing. Tomáš Suchý, PhD.; Czech Technical University in Prague; Faculty of Mechanical Engineering, Department of Mechanics, Biomechanics and Mechatronics, Technická 4, 160 00 Praha 6, Czech Republic, Tomas.Suchy@fs.cvut.cz

(CPCs), which meet the requirements of their biotolerance, biodegradability and injectability [1]. The basic CPC, which this work deals with, consists of two components (α -TCP + PLGA-PEG-PLGA). Basic CPC can be further enriched with, e.g. antibiotics, which could be applied together with bone cement directly to the site of injury, thereby would prevent the possible occurrence of infection. Although CPCs have suitable biological properties, their mechanical properties need to be optimized by the addition of other substances [2, 3].

This work deals with the evaluation of the adhesion of CPC enriched with three types of admixtures - polycaprolactone (PCL) fibers, dopamine hydrochloride, which were found to improve the mechanical properties, hardening time, and biocompatibility of cement [2] and the antibiotics vancomycin. An experimental study was performed to evaluate adhesion. There are several methods to assess the degree of adhesion, for example by methods based on the principles of fracture mechanics (three- or four-point bending), a tensile strength test or a shear strength test. The pull-out tests were chosen for the experiments in this work, the performing and preparation of the tested samples is relatively simple, and the conditions of the tests are close to the conditions of use of cements in clinical use [3]. The principle of the performed pull-out tests was the pulling out of titanium implants fixed *ex vivo* in porcine bones (specifically femurs) with cement. A total of five types of bone cement (basic CPC and its modifications with antibiotics, PCL fibers and dopamine, and PMMA as control) and two types of implants made of titanium alloy Ti6Al4V ELI, commonly used in the production of prostheses and implants, were tested. One type was implant with plasma-sprayed hydroxyapatite coating and the other type was a 3D printed implant with a trabecular surface structure. The aim of this work was to find out whether the adhesion of cement is influenced by its admixtures and types of implants and to compare the determined degree of adhesion of CPC with PMMA for which we expect a higher degree of adhesion.

2. Materials and methods

The basic evaluated adhesive was bone cement consisting of two components - the liquid component was a triblock copolymer PLGA-PEG-PLGA, and the solid part was represented by calcium phosphate (α -TCP) [1]. Modified types of cement were formed by the addition of other substances. The first type was cement with the admixture of the antibiotics vancomycin (Mylan, France), the second variant was cement with polycaprolactone (PCL) fibers (InoSPIN, InoCure, Czech Republic) and the third type was cement enriched with dopamine hydrochloride (Sigma-Aldrich, Germany) and sodium iodate (Penta, Czech Republic). The already used cement polymethylmethacrylate (PMMA), Palacos LV (Heraeus, Germany), was chosen as a control material. Both types of titanium implants (ProSpon, Czech Republic) based on Ti6Al4V ELI alloy had the shape of cylinders with a diameter of 4 mm and a length of 8 mm with an internal thread M2, but their production and surface structure differed. One type was implant with plasma-sprayed hydroxyapatite coating, the other was a 3D printed implant with a surface trabecular structure (see Figure 1). The pull-out tests consisted of pulling out implants fixed in the bone with cement. The experiments were performed *ex vivo* on 25 porcine femurs, which were shaped for experimental purposes. In the bone, it was necessary to use such places where all implants would be fixed to the always structurally identical homogeneous part of the bone, ideally to the cancellous tissue, which occurs mainly at their ends (epiphyses). Therefore, the femoral head, the proximal trochanter and both epicondyles were cut from all bones, along with the condyles, which were further divided in half - 6 different parts (marked A-F) were removed from each bone (see Figure 3).

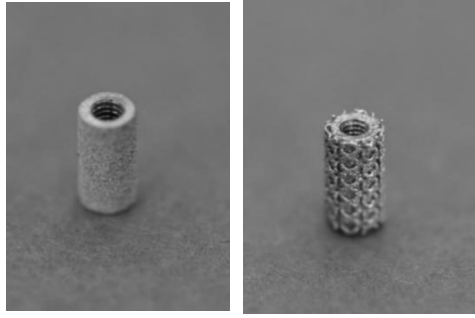


Figure 1 - Titanium implants: implant type I - with plasma sprayed HA coating (left); implant type II - 3D printed with trabecular structure (right)

The division into groups corresponds to the type of used cement, resp. used admixtures and implant type (see Table 1).

Table 1 - Overview of marking of specimen's groups

BA	basic cement	DOP	dopamine admixture
ANT	antibiotic admixture	PMMA	polymethylmethacrylate
FBR	fiber admixture		
I	HA coating	II	3D printed

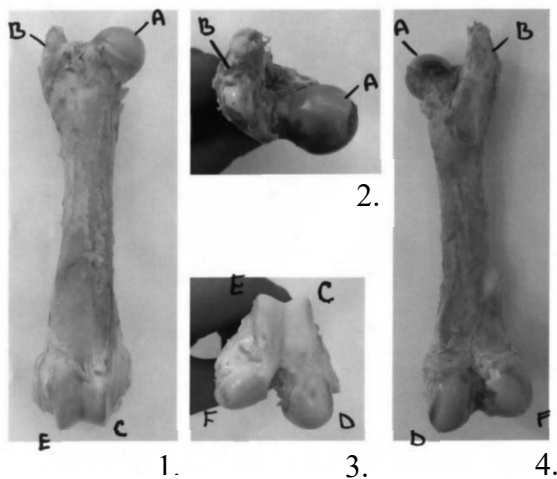


Figure 3 - Marking of bone parts for placement of implants (right femur, 1st-front, 2nd-top, 3rd-bottom, 4th-back)



Figure 2 - Test specimen (implant fixed in bone with cement)

The division of the samples into groups was designed so that each type of cement and implant was evenly represented in all bones and all their parts. A total of 110 specimens in 10 groups were tested ($n=11$).

Holes 9 mm deep and 5 mm in diameter were drilled into the excised parts of the bones into the spongy tissue so that an implant 4 mm in diameter and 8 mm in length was placed in

the hole with a clearance to create a space that would be filled with cement (simulation of placement in clinical application of cement). Cement with the volume of the entire hole was then inserted into the holes with a syringe and the implant was pressed into it so that its entire surface was surrounded by cement except for the upper surface of the cylinder (see Figure 2). The samples prepared in this way were hardened for 3 days in an incubator, where a constant temperature of 37 °C was maintained and 100% humidity was ensured with a saturated aqueous solution of copper sulphate (Penta, Czech Republic) to prevent possible development of bacteria [4].

The methodology of the experiment was based on determining the maximum force required to break the adhesion. The tests were performed on a MTS Mini Bionix test system (MTS, USA, see Figure 4) until the samples were completely pulled out at a constant speed of 10 mm/min. During the tests, time, implant displacement and force were recorded. Based on these parameters, a force-displacement diagram was compiled for each sample (see Figure 5). The maximum force required to break the adhesion F_{max} and the displacement at failure d_{max} are indicated here. Based on the maximum force, the shear strength was calculated

$$\tau = \frac{F_{max}}{S} [MPa], \text{ where} \quad 2.1$$

$$S = \pi \cdot d \cdot l [mm^2] \text{ and} \quad 2.2$$

where d is the diameter of the implant, l is its length and S corresponds to the shear surface of the implant. Figure 6 shows the force-displacement diagram of the whole group (specifically group BA II).

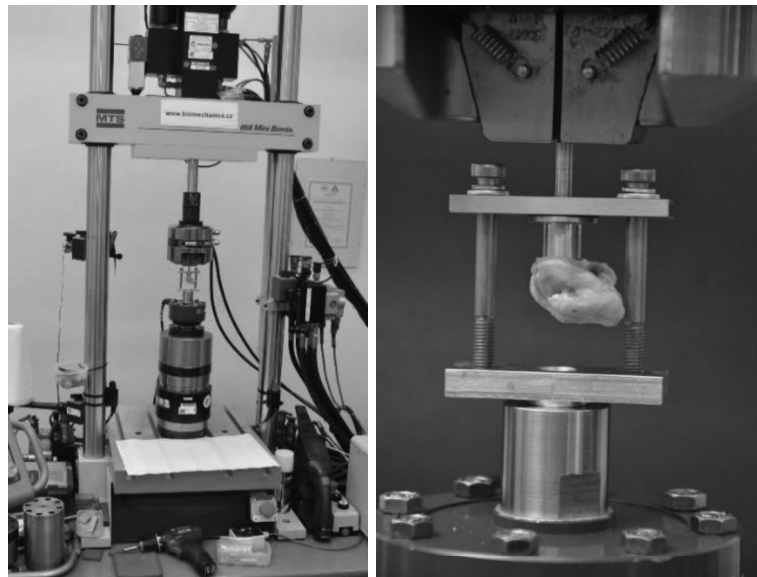


Figure 4 - MTS Mini Bionix test system (left); sample clamping detail (right)

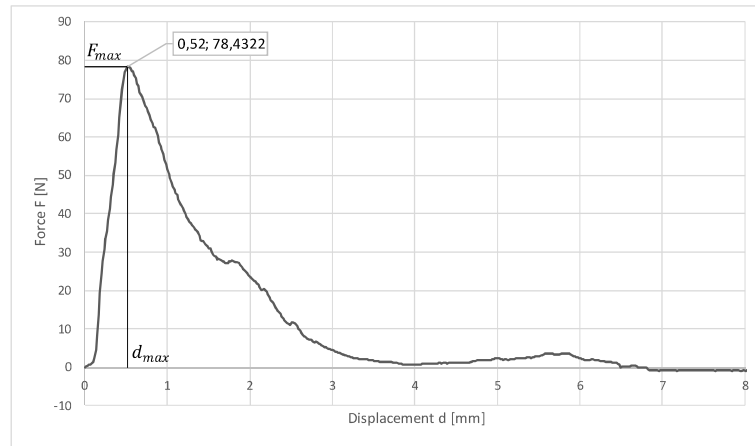


Figure 5 - Force-displacement diagram
(specimen 001 group BA II, 3D printed implant)

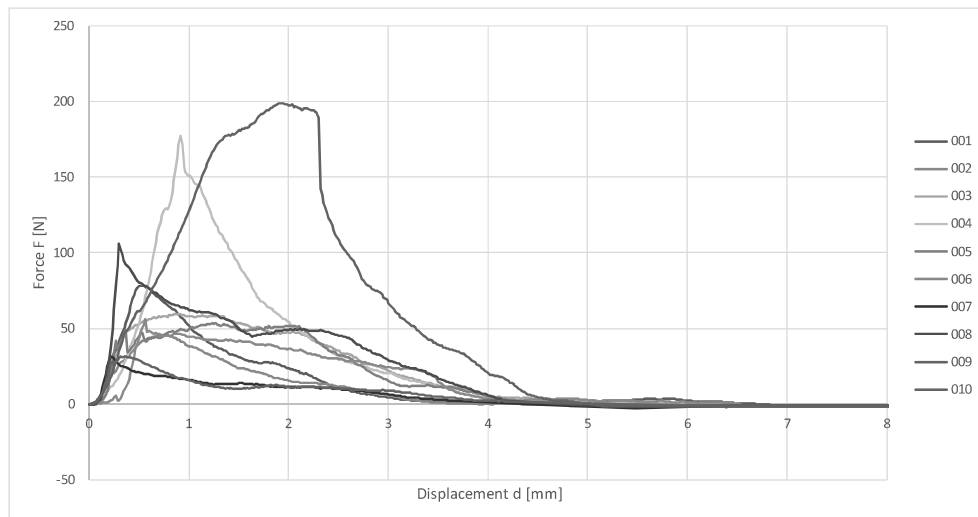


Figure 6 - Force-displacement diagram
(group BA II, specimens 001-010, 3D printed implant)

2.1. Statistical evaluation

By performing a statistical analysis, the differences of the detected values between the individual types of cement were determined, especially when using an implant type I or II. Furthermore, the influence of the type of implant used on the adhesion of each type of cement was analysed.

The statistical analysis was performed using statistical software (STATGRAPHICS Centurion XVII, StatPoint, USA). The normality of the data was verified primarily by means of the Shapiro-Wilk's test. Homoscedasticity was verified by means of the F-test (two sample comparison) or the Levene's test (multiple sample comparison). The Games-Howell test was performed for parametric multiple comparison purposes because significant differences amongst the group variances were indicated. The non-parametric Mann-Whitney W test was performed in the case of two-sample comparisons for the same reason. Statistical significance was accepted at $p \leq 0.05$.

3. Results

Table 2 shows the average values of the evaluated data for each group separately, the corresponding standard deviations and the coefficients of variation. The results of the mechanical tests are also shown together with statistical differences in the boxplots (see Figure 7 to Figure 9).

Table 2 - Summary of results (1st column – average value, 2nd column –standard deviation SD , 3rd column – coefficient of variation V for maximum force F_{max} , displacement at failure d_{max} and shear strength τ , $n=11$)

Group		$\overline{F_{max}}$	$SD_{\overline{F_{max}}}$	V	$\overline{d_{max}}$	$SD_{\overline{d_{max}}}$	V	$\bar{\tau}$	$SD_{\bar{\tau}}$	V
		[N]		[%]	[mm]		[%]	[MPa]		[%]
I	BA	83	34	39%	0,50	0,48	93%	0,76	0,32	40%
	ANT	84	29	33%	0,28	0,12	41%	0,76	0,27	34%
	FBR	82	33	39%	0,46	0,31	63%	0,76	0,31	39%
	DOP	141	62	42%	0,55	0,29	51%	1,30	0,58	42%
	PMMA	366	170	44%	1,04	0,45	41%	3,4	1,6	44%
II	BA	85	60	67%	0,77	0,52	64%	0,79	0,56	67%
	ANT	65	21	31%	0,76	0,77	97%	0,60	0,19	31%
	FBR	69	36	49%	0,62	0,71	109%	0,63	0,33	50%
	DOP	52	21	38%	0,53	0,26	46%	0,48	0,19	38%
	PMMA	280	110	36%	1,39	0,74	51%	2,6	1,0	37%

3.1. Shear strength τ and maximum force F_{max}

PMMA groups achieve the highest adhesion rates. The highest adhesion was achieved by the PMMA I group ($\tau 3.4 \pm 1.6$ MPa; $F_{max} 366 \pm 170$ N;). Statistically significant differences were found between all types of CPCs and control PMMA, using both types of implants. CPCs did not show statistically significant differences. The smallest difference occurs between the PMMA I and DOP I groups, when the adhesion rate of the DOP I group reaches 38 % of the adhesion of PMMA I.

Groups differing in the type of cement were compared, with the difference occurring only in the DOP I and DOP II groups. The DOP I group shows higher adhesion, when the adhesion rate of the DOP II group was lower by almost 63 %. This fact may be explained by the hypothesis that an implant type II has a surface with trabecular structure which forms depressions on it. Because of it, cement did not have to flow into these spaces due to its viscosity or it could get partly harden before it flows into these depressions. This would reduce the area of the implant to which the adhesive can adhere. Such a connection is then weaker than in the

case of an implant type I, where the surface of the implant is compared to II. type smooth, and therefore is the area for adhesion of the adhesive larger. The truth of the hypothesis would be confirmed by micro-CT analysis. A graphical comparison of the determined values, together with statistical differences, is shown in the figures below (see Figure 7 and Figure 8).

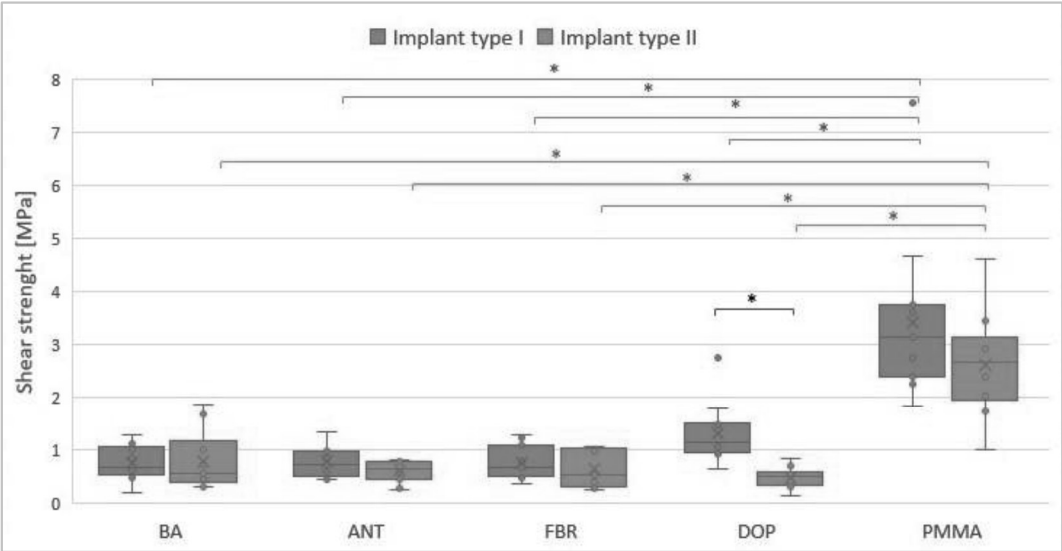


Figure 7 - Graphical comparison of specified shear stress between cement types (BA, ANT, FBR, DOP and PMMA) and implant types (I and II);
 * indicates statistically significant difference between groups (multiple comparison: G-H test, pairwise comparison: M-W test; $p \leq 0.05$, $n = 11$)

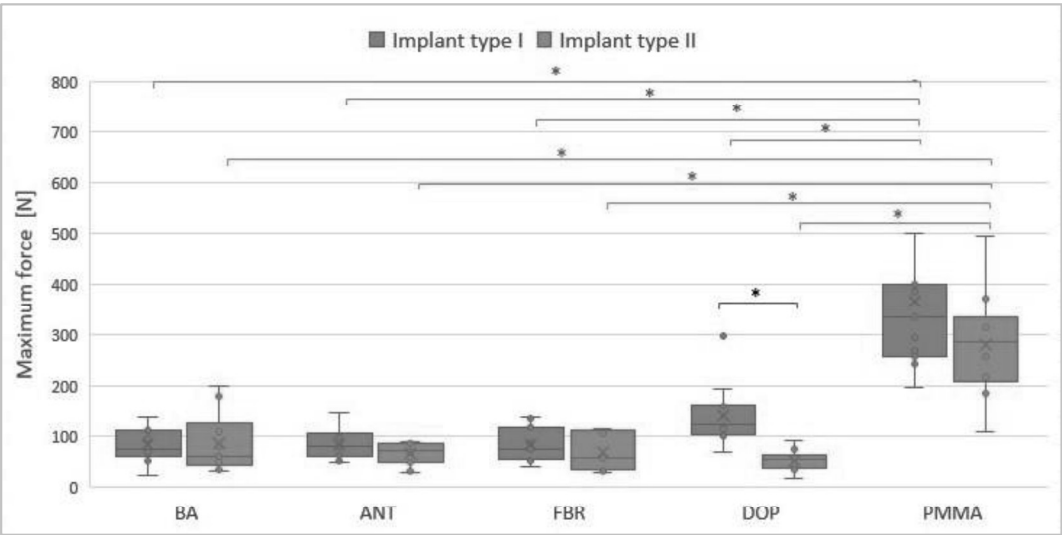


Figure 8 - Graphical comparison of specified maximum forces between cement types (BA, ANT, FBR, DOP and PMMA) and implant types (I and II);
 * indicates statistically significant difference between groups (multiple comparison: G-H test, pairwise comparison: M-W test; $p \leq 0.05$, $n = 11$)

3.2. Displacement at failure d_{max}

The highest values of displacement at failure were obtained by the PMMA groups, the maximum value belongs to the PMMA II group (1.39 ± 0.78 mm). Statistical analysis showed that the displacement at failure differs only in the implant type I samples compared to the PMMA I group in the BA I, ANT I and DOP I groups. The smallest difference occurs between the DOP I and PMMA I groups, when the displacement at failure of DOP I group is lower by only about 47%. A graphical comparison of the determined values, together with statistical differences, is shown in the figure below (see Figure 9).

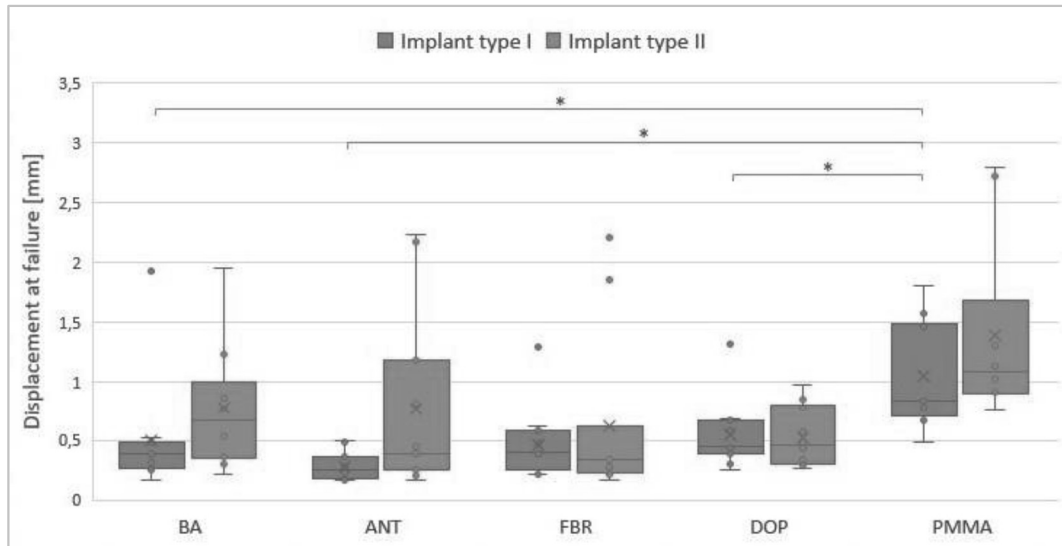


Figure 9 - Graphical comparison of determined displacements at failure between cement types (BA, ANT, FBR, DOP and PMMA) and implant types (I and II); * indicates statistically significant difference between groups (multiple comparison: G-H test, pairwise comparison: M-W test; $p \leq 0.05$, $n = 11$)

4. Conclusion

The highest adhesion rates were shown by the PMMA I and PMMA II groups, as expected. Of the modified CPCs, the DOP I group performed best in tests, with a shear strength reaching 38 % of value of the PMMA I, as well as a maximum force value. Value of displacement at failure is only 47 % lower than PMMA I. By comparing the DOP I group with the DOP II group, we find that DOP I shows 63% better adhesion than the DOP II group. The results obtained suggest that the addition of dopamine increases the adhesion of cement when applied using a hydroxyapatite coated implant (type I).

Based on the performed tests and statistical analysis, we can conclude that PMMA evinced the highest quality of adhesion compared to other types of cement. As it was mentioned in the introduction, the materials today commonly used in surgery have certain disadvantages and their replacement or improvement is being sought. Although commonly used PMMA cement is tolerated by the body, it does not cause an immunological reaction, but its disadvantage is the inability to degrade, the inability to inject it into the wound site, and it heats up during hardening. In this point of view, we can consider more suitable the remaining types of cements, which are biotolerant, biodegradable, injectable, do not heat up and their degree of adhesion does not deteriorate by adding admixtures. Although the results show a lower rate of

adhesion of the developed CPC, the observed decrease in the initial healing phase may not be limiting for specific applications.

5. Acknowledgement

This study was supported by the grant project awarded by the Ministry of Health of the Czech Republic No. NV18-05-00379.

References

- [1] VOJTOVA, Lucy, Lenka MICHLOVSKA, Kristyna VALOVA et al. The Effect of the Thermosensitive Biodegradable PLGA–PEG–PLGA Copolymer on the Rheological, Structural and Mechanical Properties of Thixotropic Self-Hardening Tricalcium Phosphate Cement. *International Journal of Molecular Sciences* [online]. 2019, **20**(2), 1-21 [cit. 2020-11-02]. ISSN 1422-0067. Available from: doi:10.3390/ijms20020391
- [2] CALORI, G.M., E. MAZZA, M. COLOMBO a C. RIPAMONTI. The use of bone-graft substitutes in large bone defects: Any specific needs?. *Injury* [online]. 2011, **42**, 56-63 [cit. 2020-11-24]. ISSN 00201383. Available from: doi:10.1016/j.injury.2011.06.011
- [3] BÖKER, Kai O., Katharina RICHTER, Katharina JÄCKLE et al. Current State of Bone Adhesives—Necessities and Hurdles. *Materials* [online]. 2019, **12**(23) [cit. 2020-11-08]. ISSN 1996-1944. Available from: doi:10.3390/ma12233975
- [4] VLTAVSKÝ, Martin. *Analýza mechanických vlastností porézních keramických pěn pro náhrady kostní tkáně při akcelerované degradaci*. Praha, 2020. Diplomová práce. České vysoké učení technické v Praze.
- [5] ERHART, S., W. SCHMOELZ, M. BLAUTH a A. LENICH. Biomechanical effect of bone cement augmentation on rotational stability and pull-out strength of the Proximal Femur Nail Antirotation™. *Injury* [online]. 2011, **42**(11), 1322-1327 [cit. 2020-11-10]. ISSN 00201383. Available from: doi:10.1016/j.injury.2011.04.010
- [6] BENHALIMA, Lamia, Sandra AMRI, Mourad BENSOUILAH a Rachid OUZROUT. Antibacterial effect of copper sulfate against multi-drug resistant nosocomial pathogens isolated from clinical samples. *Pakistan Journal of Medical Sciences* [online]. 2019, **35**(5) [cit. 2021-04-15]. ISSN 1681-715X. Available from: doi:10.12669/pjms.35.5.336

EFFECT OF METALLIC PLATE FIXATION ON MECHANICAL PROPERTIES OF REGENERATED RIB FRACTURES

Kristýna Kubášová¹, Radek Sedláček¹, Lucie Vištejnová², Maria Štěpánková³ & Pavel Klein²

Abstract: This work deals with the influence of the plate on the mechanical properties of the fracture of explanted pork ribs. The methodology of the experiment was based on the determination of the maximum force and maximum bending stress needed to break the rib at a three-point bend. Other mechanical parameters were evaluated (bending stiffness, maximum bending moment, maximum deflection, etc.). A total of 9 samples were tested from 4 experimental animals. The analysis was focused on comparison of the parameters evaluated from measured data of the ribs supported by the plate and the ribs without the plate fixation. These evaluated data were statistically analyzed.

1. Introduction

The development of surgical methods and modern fixation devices focuses, among other things, on operative therapy of segmental fractures. Surgical treatment of fractures of the rib segment provides several benefits that result from improved chest wall stabilization, such as improved respiratory parameters, shorter recovery times and lower costs compared to conservative therapy [1]. However, some authors and doctors are still in favor of conservative therapy. The question is therefore whether treatment by fixation of the metal plate interferes with the healing process of the surrounding tissue due to disruption of the bone surface and vascular supply [2].

In this project, we deal with the effect of metal plate fixation on the healing of pig's ribs fractures. A total of 8 experimental animals were treated by the plate fixation, 2 experimental animals were treated conservatively (control group). Three weeks after surgery, the ribs were explanted and divided into groups for other experiments. In our biomechanical experiment, a total of 9 samples from 4 experimental animals were tested. The main objective of the project is to evaluate the effect of plate fixation on the regeneration process of rib fracture by mechanical testing.

2. Methods and Materials

The methodology of the experiment was based on the determination of the maximum force and maximum bending stress needed to break the rib at a three-point bend. Other evaluated parameters were bending stiffness, maximum bending moment, maximum deflection,

¹ Ing. Kristýna Kubášová, Ing. Radek Sedláček, Ph.D.; Czech Technical University in Prague, Faculty of Mechanical Engineering, Department of Mechanics, Biomechanics and Mechatronics, Technická 4, 160 00 Praha 6, Czech Republic; Kristyna.Kubasova@fs.cvut.cz, Radek.Sedlacek@fs.cvut.cz

² Ing. Lucie Vištejnová, Ph.D., Ing. Pavel Klein, Ph.D.; Charles University, Medical Faculty in Pilsen, Biomedical Center, alej Svobody 1655/76, 301 00 Plzeň, Czech Republic; lucie.vistejnova@lfp.cuni.cz, pavel.klein@lfp.cuni.cz

³ MUDr. Maria Štěpánková; Klinik für Thoraxchirurgie, Fachkliniken Wangen, Am Vogelherd 14, 88239 Wangen im Allgäu, Germany; stepankov.maria@gmail.com

deformation energy into destruction and force and deflection at yield strength. The samples were tested on a special 3-point bending fixture, at a constant feed 5 mm/min. Displacement, time and maximum force were recorded with the sampling frequency 40 Hz.

A total of 9 explanted rib samples were tested in two experiments (see Figure 1). The samples were divided into two groups – group A contains 5 rib samples after fixation by a plate and group B contains 4 rib samples regenerated without a plate (see Table 1). All samples were tested without plates. The distance between the support rollers with a diameter of 4 mm was $r = 38$ mm.

The MTS Mini Bionix 858.02 (MTS, Minnesota, USA) system with a load cell (with a range of 0 ÷ 500 N) and a special fixture made for this type of test (see Figure 2). we used for experiments.



Figure 1: Tested samples

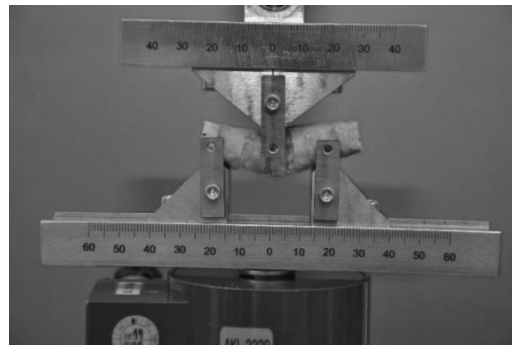


Figure 2: Power sensor and a special fixture made for this type of test

Table 1: Classification and labeling of sample group

Sample number	Group	Characteristic	Original sample identification
1	Group A	Ribs with fixation by plate	Z2_5
2			Z2_6
3			Z2_7
8			Z4_4
9			Z4_5
4	Group B	Ribs without fixation by plate	Z1_2
5			Z1_5
6			Z3_2
7			Z3_5

Note: Red highlight – Sample 7_Z3_5 has been delivered in damaged state. Therefore, the sample was excluded from further evaluation.

3. Results

Firstly, the samples of the elliptical cross-section were measured. Both half-axes, length and the section modulus W_{Oz} were recorded in the table for further evaluation. The data recorded during the experiment were processed into graphs with force – deflection curve. Other parameters were evaluated from relations based on bending experiment. The yield strength and deflection at yield strength were determined as the value at the intersection of the 0,1 mm offset of the tangent of the linear phase. The deformation energy is determined as the maximum energy required for the destruction of the sample, i.e. into the maximum force. The graph with curve of the bending stress – deflection was created for all tested samples (see Figure 3). The table (see Table 2) summarizes all parameters and their arithmetic means.

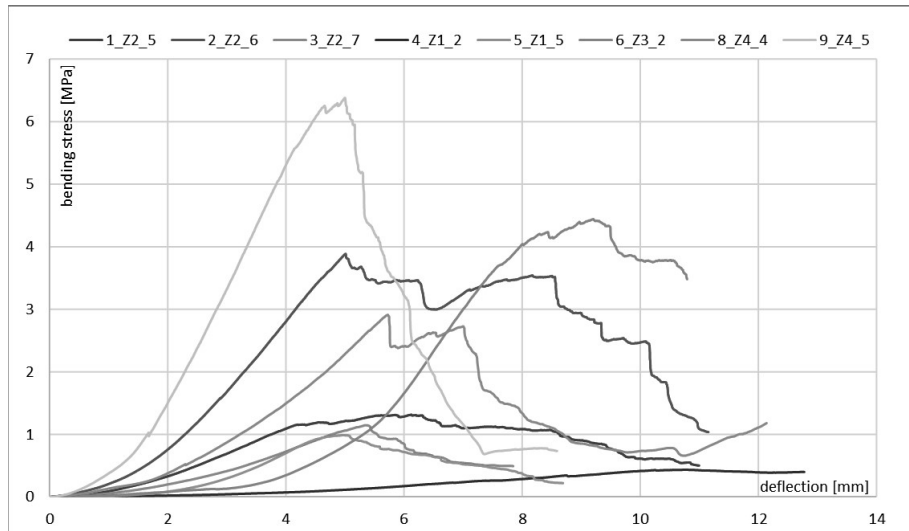


Figure 3: Summary graph of bending stress on the deflection

The maximum force for samples after plate fixation was lower than for samples without the plate, the maximum bending stress is higher for samples treated by the plate (see Table 2).

Table 2: Arithmetic means of evaluated parameters

Evaluated parameters		A	B
Maximum deflection	v_{max} [mm]	5,34	8,32
Maximum force	F_{max} [N]	52,65	108,81
Maximum bending moment	$M_{o_{max}}$ [N·mm]	500,20	1033,74
Maximum bending stress	σ_{max} [MPa]	3,14	1,96
Bending stiffness	EJ [N·mm ²]	362888	508832
Deformation energy	U [N·mm] = [J]	140,31	456,46
Yield strength	F_{σ_k} [N]	36,91	132,40
Deflection at yield strength	v_{σ_k} [mm]	4,70	6,19

The arithmetic means and other statistical indicators of maximum force and maximum bending stress are shown in the statistical graphs below (see Figure 4).

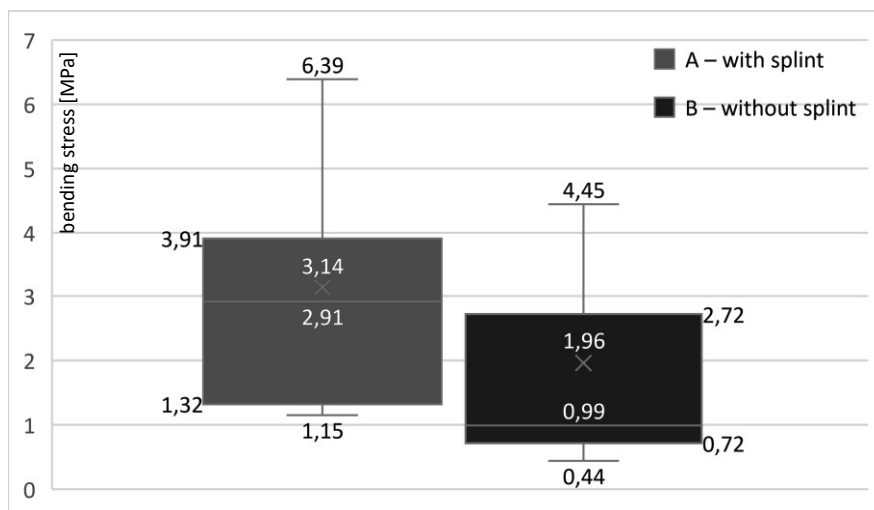


Figure 4: Statistical graph (box plot) of maximum bending stress

Data were tested by Shapiro-Wilk test of normality. It is apparent from the table below that all data comes from a normal distribution (see Table 3). Student's T-test (see Table 3) was used to compare the statistical significance of the differences between these two groups (the assumption of normal distribution applies). Although the difference in mean values of maximum force is twice as large, and the difference in maximum bending stress of samples without a plate is by one-third lower, there was no significant difference in the T-test. Not even for other evaluated parameters. This is probably due to the small number of tested samples in each group (i.e. 5 samples – with plate and 3 samples – without plate).

Table 3: Statistical evaluation

Statistical test		Normal distribution (Shapiro-Wilk test)		Significant difference (Student T-test)
		0 = no, 1 = yes		0 = no, 1 = yes
		A	B	A / B
Maximal deflection	v_{max}	1	1	0
Maximal force	F_{max}	1	1	0
Maximal bending moment	$M_{o\ max}$	1	1	0
Maximal bending stress	σ_{max}	1	1	0
Bending stiffness	EJ	1	1	0
Deformation energy	U	1	1	0

4. Conclusion

The following parameters were determined for the three-point bending test: maximum force, maximum bending stress, bending stiffness, maximum deflection, deformation energy to destruction and force with deflection at yield strength. A total of 9 samples were divided into two groups. One sample was eliminated for its damaged state before testing.

Obtained data were statistically evaluated. The maximum force from group A (after plate fixation) was lower than from samples of group B (without the plate). Meaning that lower pressure force is needed for the rib destruction. On the other hand, the maximum bending stress is higher for samples from group A. This is because to the larger cross-sectional area of the samples without plate fixation. But there was no significant difference in the statistical tests for all measured parameters. We believe that further experiments with a larger number of samples will result in our conclusions being also supported by statistical significance.

5. Acknowledgements

The project was supported by Charles University Grant Agency, grant number 1468218 and the SGS, with grant number SGS19/155/OHK2/3T/12.

References

- [1] Althausen PL, Steven Sahnnon BS, et al. Early stabilization of flail chest with locked plate fixation. J Orthop Trauma.2011; 25(11): 641-647
- [2] Solberg BD, Moon CN, Nissim AA, et al. Treatment of chest wall implosion injuries without thoracotomy: technique and clinical outcomes. J Trauma. 2009; 67:8–13.

INFLUENCE OF TEMPERATURE INCREASE ON YOUNG MODULUS OF ELASTICITY OF CFRP

Martin Matuš¹, Bohumil Kropík², Karel Doubrava³, Milan Růžička⁴ and Jan Řezníček⁵

Abstract: Tensile testing and evaluation of theoretical mechanical properties of carbon fiber reinforced polymers were measured and computed at room temperature. This study investigates the effect of higher temperature on the mechanical properties of carbon fiber reinforced polymers. Mechanical properties were measured via tensile testing using a strain gauge. This work is focused on comparing the modulus of elasticity at three different levels of temperature, the first level is the room temperature, the second level is 60°C, and the highest temperature is 100°C. Our measurements confirm the assumption that the mechanical properties are changing with increasing temperature.

1. Introduction

Fiber Reinforced Polymer (FRP) composites are commonly applied to improve conventional constructions made from metals. FRP's could be divided into groups by type of used fiber, for example, Glass Fiber Reinforced Polymers (GFRP), Aramid Fiber Reinforced Polymers (AFRP), or Carbon Fiber Reinforced Polymers (CFRP). Our interest was especially in CFRP, which are composites massively used for lightening and strengthening constructions. Types of carbon fibers could be divided into two groups, for example, by the type of precursor on Pitch and PAN. PAN fibers are characterized by High Strength (HS) and Pitch fibers are characterized by very high modulus of elasticity as so-called Ultra High Modulus fibers (UHM) [1] [2].

With the application of conventional materials which are homogeneous, and their properties are known, the influence of temperature on their mechanical properties is well described too. For carbon fiber reinforced polymers, there are measurements which are suggesting a slight decrease of stiffness and strength at much higher than room temperature [3] and an increase at lower temperatures than zero [4].

The main objective of this work is to establish whether the increase of temperature is reducing the stiffness of the composite material. In other words, to determine if there could be said that the mechanical properties of the composite are invariant to the surrounding temperature or not.

¹ Ing. Martin Matuš; Czech Technical University in Prague, Department of Mechanics, Biomechanics and Mechatronics, Technická 4, 1600 Prague, Czech Republic, martin.matusu@fs.cvut.cz

² Ing. Bohumil Kropík; Czech Technical University in Prague, Department of Mechanics, Biomechanics and Mechatronics, Technická 4, 1600 Prague, Czech Republic, bohumil.kropik@fs.cvut.cz

³ Ing. Karel Doubrava, Ph.D.; Czech Technical University in Prague, Department of Mechanics, Biomechanics and Mechatronics, Technická 4, 1600 Prague, Czech Republic, karel.doubrava@fs.cvut.cz

⁴ prof. Ing. Milan Růžička, CSc.; Czech Technical University in Prague, Department of Mechanics, Biomechanics and Mechatronics, Technická 4, 1600 Prague, Czech Republic, milan.ruzicka@fs.cvut.cz

⁵ doc. Ing. Jan Řezníček, CSc.; Czech Technical University in Prague, Department of Mechanics, Biomechanics and Mechatronics, Technická 4, 1600 Prague, Czech Republic, jan.reznicsek@fs.cvut.cz

2. Preparation of testing

2.1 Specimens

Specimens were made of HS carbon fibers and epoxy polymer matrix (LG900UV/HG100). Production method of filament winding on a mandrel of square cross-section shape that was cut into four plates sized 1000 x 120 mm and thickness of 5 mm was used. Specimens were then cut into plates of dimension 200 x 40. The composite lay-up is described in Tab 1.

On each specimen, two linear uniaxial strain gauges (HBM 1-LY41-6/350) were installed, one on both sides, to assess the impact of additional bending of specimens. On one sample, four strain gauges were installed for determining Poisson's ratio. Except for one specimen where the strain gauge was applicated with HBM EP310N [5] (adhesive with thermal resistance up to 310 °C) all specimens were applicated with Kyowa CC-33A [6] adhesive (Fig. 1) with thermal resistance up to 120 °C. Installing of SG's with Kyowa adhesive is faster and the thermal resilience of epoxy polymer matrix which was used for our specimens is up to 150 °C so we decided to measure at the highest level of 100 °C.

Table 1: Composition of CFRP specimens

Layer Number	Fibre Volume Fraction (%)	Layer Thickness (mm)	Winding Angle (°)
1	58	0,612	46
2	58	0,241	89
3	58	0,609	46,3
4	58	0,606	46,5
5	58	2,183	0
6	58	0,596	47,6

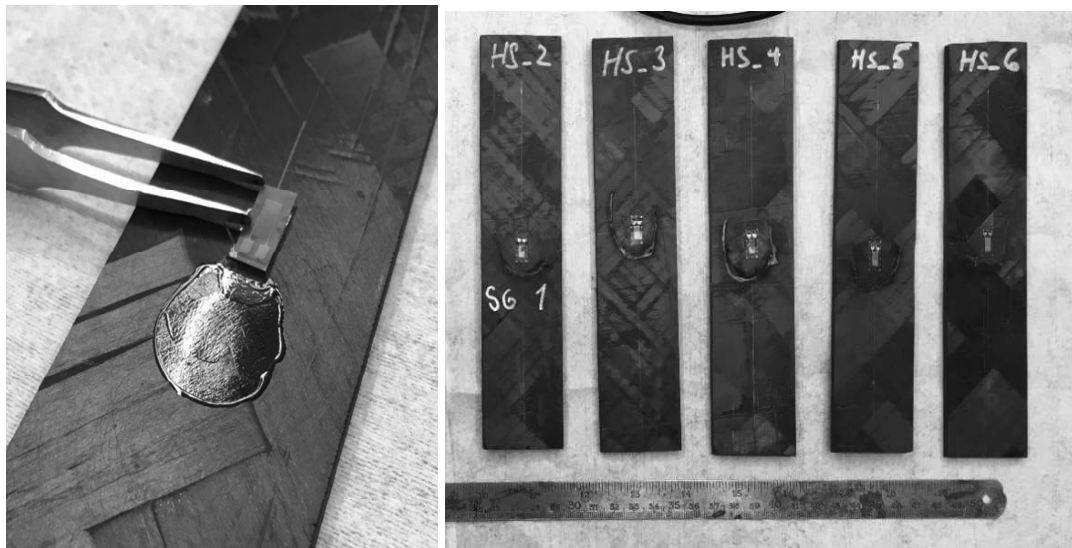


Figure 1: Application of strain gauge to composite plates.

2.2 Measuring equipment

Measuring was held on a universal electromechanical tensile/compression testing machine Tira 2300 with the use of a thermal chamber with range -100 °C to 350 °C produced by

LaborTech (Fig. 2). All measurements were recorded on QuantumX M1615B with 50 Hz sample rate.

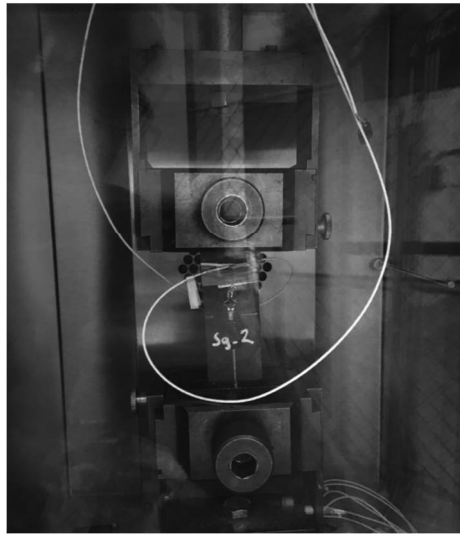


Figure 2: Sample held in mechanical jaws in LaborTech thermal chamber.

2.3 Measurement procedure

All specimens were loaded with relatively low force due to the repeatable examination of each sample, finding that the forces are in the Very High Cycle Fatigue (VHCF) region of fatigue, hence the possibility of damage the specimens was minimal. Testing was conducted in range between 1 kN and 10 kN three times, then the specimen was changed. Experiment was measured at three levels of temperature, 20 °C, 60 °C and 100 °C.

All specimens were exposed to a constant level of temperature for at least 6 hours before measuring. Between measuring of specimens were at least 15 min intervals to heat up the inner surroundings of heat chamber for a consistent environment for each measurement.

The main point of interest was to measure the tensile strain on each sample to give us an overview on the mechanical properties in each level of thermal exposure.

3. Evaluation

With the use of quarter-bridge connection of strain gauges on each side, the bending component of strain (ϵ_{θ}) and tensile component of strain (ϵ_T) were evaluated from measured strain as indicated in Fig. 3 with use of equations (1) and (2). This set-up was used to eliminate additional bending. Measuring with only one strain gauge on a side was proven to be insufficient.

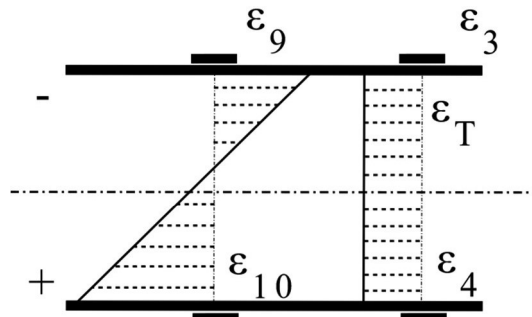


Figure 3: Evaluation scheme with strain gauge's on tubular shape specimen.

$$\varepsilon_O = \frac{\varepsilon_{10} - \varepsilon_9}{2} \quad (1)$$

$$\varepsilon_T = \frac{\varepsilon_4 + \varepsilon_3}{2} \quad (2)$$

Young modulus of elasticity was evaluated six times on one specimen for each measured thermal level for better results and to give us an overview on any occurring hysteresis. Modulus of elasticity was computed between 4 kN and 5,5 kN for each loading cycle. In Fig. 4, the points in which the modulus of elasticity was measured. Then a mean value was established for each loading and unloading cycle and from the six mean values an average was made to give us a Young modulus of elasticity at each thermal level for one specimen.

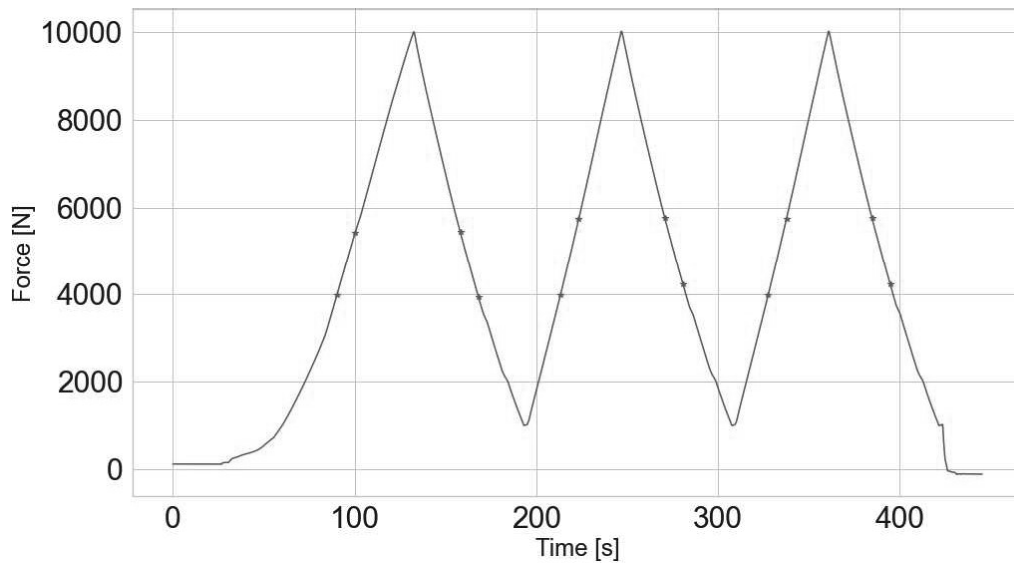


Figure 4: Three cycles at temperature level of 20°C with marked points for evaluation on sample HS_5.

4. Results

Based on our testing, there was a minor decrease of Young modulus of elasticity with higher temperature than room temperature. This could be used in FEM analysis of composite construction to give us a more accurately designed model.

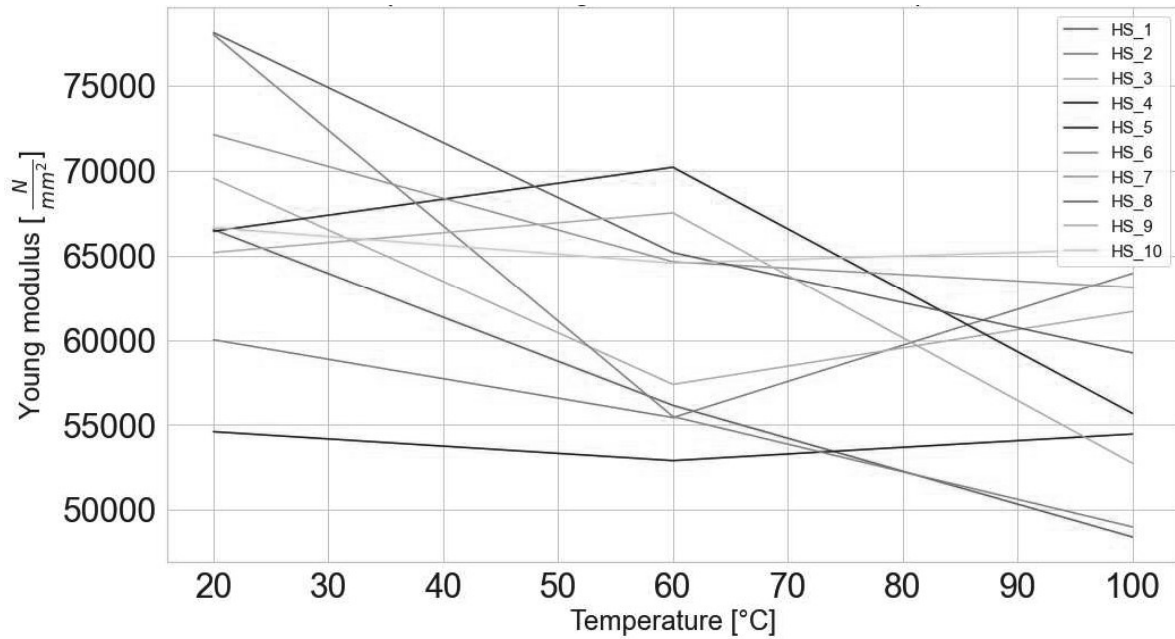


Figure 5: Linear estimation of Young modulus with regard on temperature.

Decrease of Young modulus of elasticity of the composite made of epoxy matrix reinforced with HS carbon fibers regarding room temperature was 10 % at temperature level of 60 °C and 15 % at temperature level of 100 °C which is significant according to T-test (all distributions were Gaussian so the T-test could be made). The decrease of Young modulus can be seen from Fig. 5 which displays the mean value of Young modulus of elasticity for each thermal level and each specimen. For better visibility, the box plot was made (Fig.6) where the mean value is represented by the orange line in box.

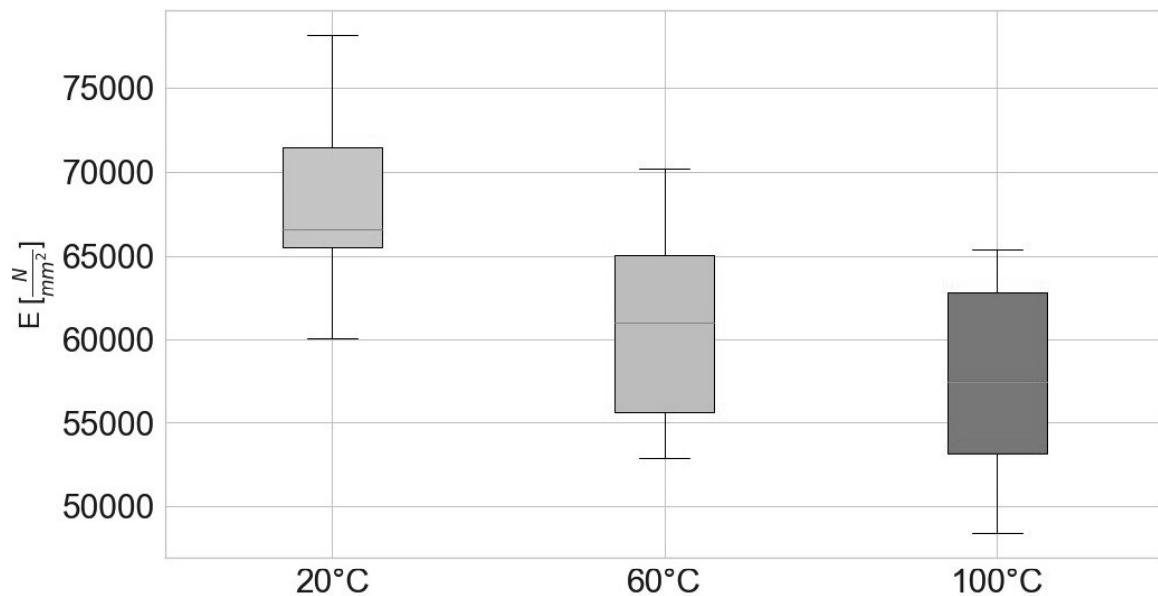


Figure 6: Distribution of Young modulus regarding to temperature.

5. Conclusion

This work describes an experiment with CFRP specimens under increased temperature exposure subjected to tensile testing. As a conclusion from this work, it can be said that the Young modulus of elasticity depends on the temperature of environment. The stiffness of measured CFRP is not invariant to temperature. The Young modulus of elasticity decreased within increasing temperature. From our measuring, the rate of decrease is 10 % of Young modulus with the change of temperature to 60 °C and 15 % with the increase of temperature to 100 °C from room temperature of 20 °C. This conclusion could be implemented into FEM model for more accurate design of composite construction.

This fact comes to an agreement with other works on this topic. In the future, measuring level of temperature will be under room temperature and near to the glass transition temperature of used matrix. Moreover, results comparing HS and UHM would be useful.

6. Acknowledgement

This work has been supported by the Grant Agency of the Czech Technical University in Prague, under grant No. SGS21/151/OHK2/3T/12 and supported by NCC MESTEC (National Competence Centre of Mechatronics and Smart Technologies for Mechanical Engineering), under project No. TN01000071

References

- [1] EHRENSTEIN, G. W. *Polymerní kompozitní materiály*, Scientia, ISBN 978-80-86960-29-6, Prague, (2009)
- [2] LAŠ, V. *Mechanika kompozitních materiálů*, University of Western Bohemia, ISBN 978-80-7043-689-9, Pilsen, (2008)
- [3] YANG, Y., JIANG Y., LIANG H., YIN X. and HUANG Y., Study on Tensile Properties of CFRP Plates under Elevated Temperature Exposure, *Materials*. **Vol.** 12. 2019, 12(12). ISSN 1996-1944.
- [4] JIAN Z., LI T., CHIANG F., WANG L., An experimental investigation of the temperature effect on the mechanics of carbon fiber reinforced polymer composites, *Composites Science and Technology* **Vol.** 154. 2018, ISSN 02663538
- [5] *EP310N: Hot Curing Adhesive for Smooth Surfaces or for Thin Layers*, HBM, Available from: <https://www.hbm.com/en/2959/ep310n-two-component-epoxy-resin-adhesive/> , Accessed: 2021-04-12
- [6] *Adhesives and Bonding Tools: Kyowa CC-33A*, Kyowa, Available from: https://www.kyowa-ei.com/eng/product/category/strain_gages/s_adhesive/index.html , Accessed: 2021-04-12

EXPERIMENTAL DEVICE FOR APPLICATION OF REINFORCEMENT LEARNING ALGORITHMS TO PNEUMATIC SPRINGS

Jiří Rágulík¹ & Michal Sivčák²

Abstract: This paper describes the creation of an experimental jig to apply enhanced learning algorithms to a pneumatic spring. It also describes the advantages of learning algorithms on a real spring compared to learning on a mathematical model.

1. Introduction

In our previous contributions, a mathematical model of a pneumatic bellows spring was created, and the height of this spring was regulated by a PID controller [Rágulík, Sivčák 2019], which was set by the method Ziegler-Nichols. PID control gives relatively good results due to the simplicity of setting the gain of individual components of the controller. The Deep Deterministic Policy Gradient (DDPG) [Lilicrap 2015] algorithm was chosen as the successor to the PID controller [Rágulík, Sivčák 2020]. The operation of a group of actor-critic algorithms, including our chosen algorithm, is shown in the following (Figure 1).

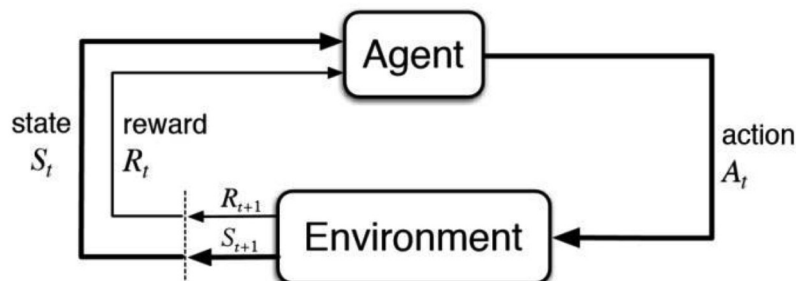


Figure 1: Scheme of reinforcement learning algorithms [4].

The agent (DDPG algorithm) makes action interventions into the environment (mathematical model of a pneumatic spring) and receives as feedback the state to which the environment got after the action was performed and a reward that provides the agent with information about the quality of the action. In this case, the reward function used depends on the deviation of the required and actual spring height and the pressure inside the spring bellows. At zero deviation, the agent receives the maximum reward. On the contrary, the agent receives a negative reward, a penalty, for changing the pressure too quickly, thus preventing the agent from learning to switch between zero and maximum possible pressure only with a certain frequency, which leads to a high reward for the mathematical model of the spring used. However, in reality, such a procedure is very inappropriate and energetically disadvantageous. The mentioned mathematical model was created in Simulink (Figure 2) for the purpose of learning the algorithm, while

1 Jiří Rágulík; Technical University of Liberec; Studentská 2, 461 17 Liberec, Czechia, jiri.ragulik@tul.cz

2 Michal Sivčák, Ph.D.; Technical University of Liberec; Studentská 2, 461 17 Liberec, Czechia, michal.sivcak@tul.cz

the algorithm itself runs in Matlab. To achieve high quality of regulation, we want to learn the algorithm directly on the physical spring.

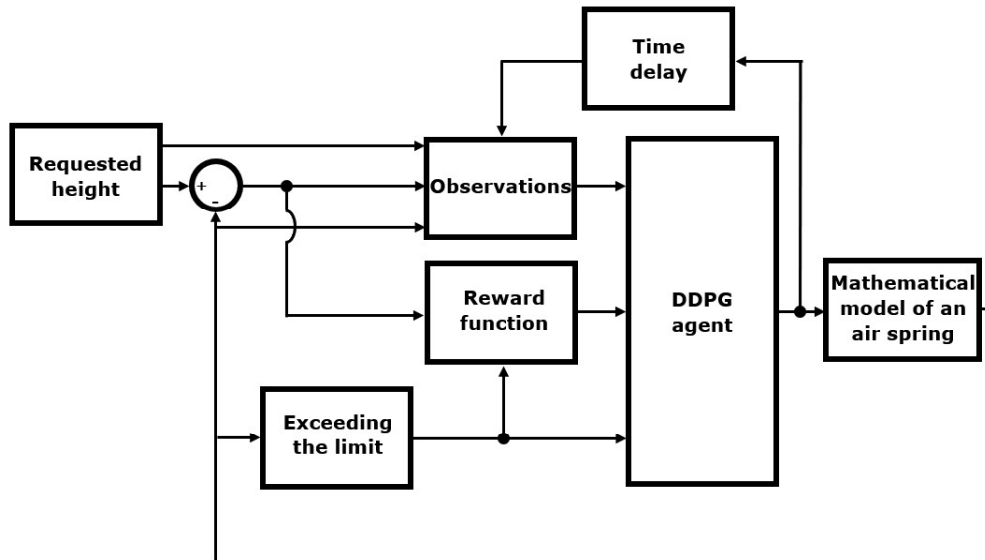


Figure 2: Scheme of DDPG algorithm created in Simulink.

The mathematical model achieves a deviation of approximately 5 % in the working area of the spring. With a rapidly changing load, a higher inaccuracy of the model can be assumed, in which the changes taking place in the bellows of the spring are considered to be isothermal and reversible. With a rapidly changing load, greater changes in the air temperature in the spring will occur, and the process can therefore no longer be considered isothermal. In finding the optimal transfer function, represented by a sufficiently large deep neural network, the algorithm should learn by learning a transfer function taking into account the mentioned phenomena not included in the mathematical model of a pneumatic spring, such as rubber relaxation of a spring bellows. We make this assumption based on the validity of Kolmogor's theorem, which states that every real multidimensional function of n variables can be accurately expressed as a linear combination of a finite number of continuous nonlinear functions of one variable. In the case of neural networks, these nonlinear functions are realized by an activation function in each neuron. In our case, it is a Rectified Linear Unit (ReLU) function.

2. Experimental device

The device must allow the loading of the spring, namely static loading in the form of weights, but also dynamic loading caused by external excitation. Furthermore, it must allow the measurement of the length of the spring by a laser sensor, the supply of compressed air to the spring, and the regulation of the air pressure inside the spring bellows by a pressure regulator.

The frame was made of aluminum profiles and a linear guide. The only assumed direction of the force load is the direction of the linear guide, so there were no special requirements for the rigidity of the jig. The jig had to allow the spring stroke in the range of 85 to 140 mm, to which it was still necessary to add the height of the washer to clamp the spring to the base of the frame. A modular linear guide roller system was chosen. It is characterized by stroke length, high load capacity, low resistance, and high travel speed. The running logs are hardened and ground and are pressed into their holders. A washer was created using 3D printing technology to clamp the spring. The connection of the spring with the washer is secured by two screws, the attachment of the washer to the experimental jig is secured by four screws. The height of the washer was chosen with respect to the height of the pneumatic elbow, through which compressed air is supplied to the bellows of the clamped spring. A laser sensor holder was also made using 3D printing technology. No forces act on the laser sensor, so the holder only serves

to secure the position of the sensor. Both parts made by 3D printing technology were made of polylactic acid (PLA).

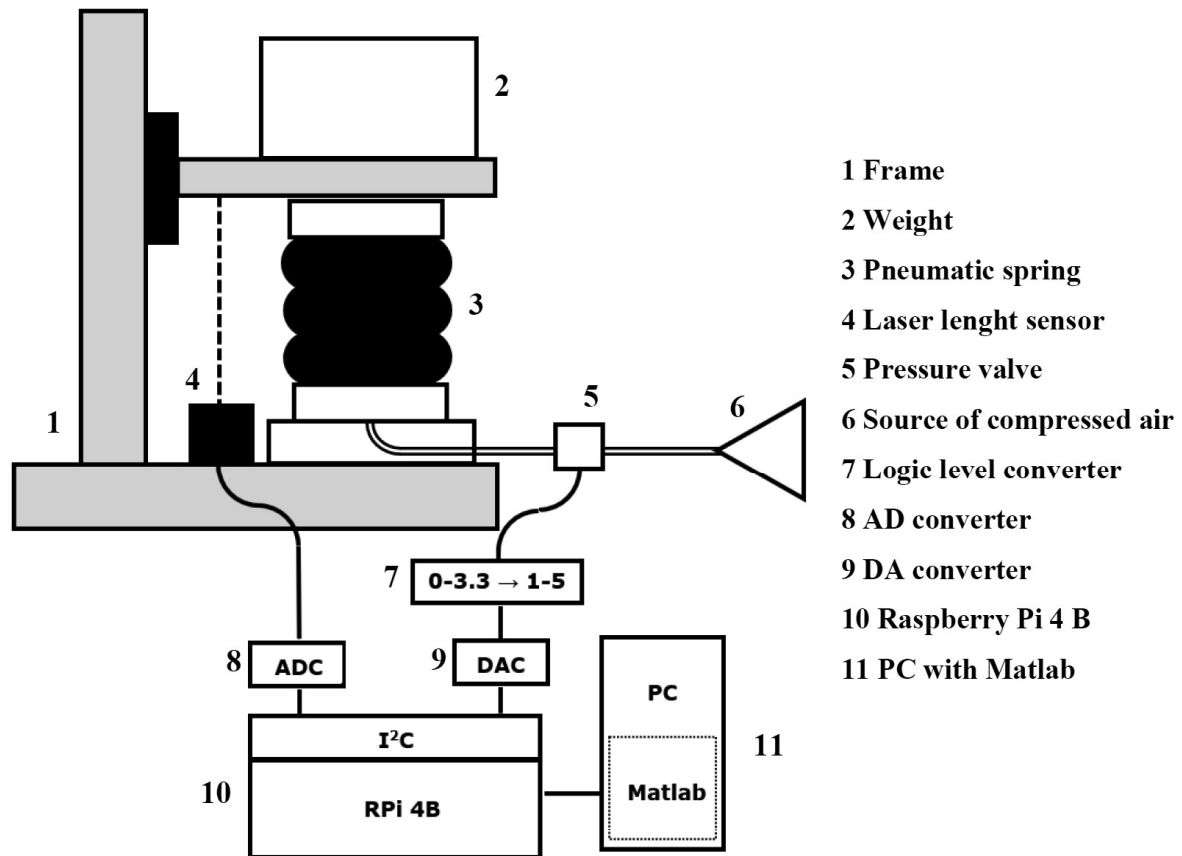


Figure 3: Scheme of the experimental device, including

A laser length sensor optoNCDT 1402-200 was used to obtain spring stroke information. A pressure valve SMC VY1A00 was used to control the pressure inside the spring bellows. The sensor gives stroke information in the form of a DC voltage in the range of 1 to 5 V. the same voltage range controls the pressure valve. The Raspberry Pi 4 model B, which operates in the voltage range 0 to 3.3 V, was used as a mediator in communicating the algorithm in Matlab with the sensor and the valve. It was necessary to convert the analog signal from the length sensor to a digital signal, processable by Raspberry Pi. An 16-bit AD converter ADS 1100 was used for this purpose. On the contrary, the digital signal for controlling the pressure valve had to be converted to an analog signal. A 12-bit DA converter MCP 4725 was used for this purpose. Data from the converters are fed to the Raspberry Pi via the I2C interface. SPI and I2C interfaces are usually used for similar purposes. In our experimental product, the I2C interface was chosen, which is less prone to noise and requires fewer wires (SDA for data and CLK for the clock) than SPI (usually 4 wires), which significantly simplifies the connection. On the other hand, the SPI interface is approximately twice as fast [Visconti 2017]. The speed of the I2C interface proved to be sufficient in this case.

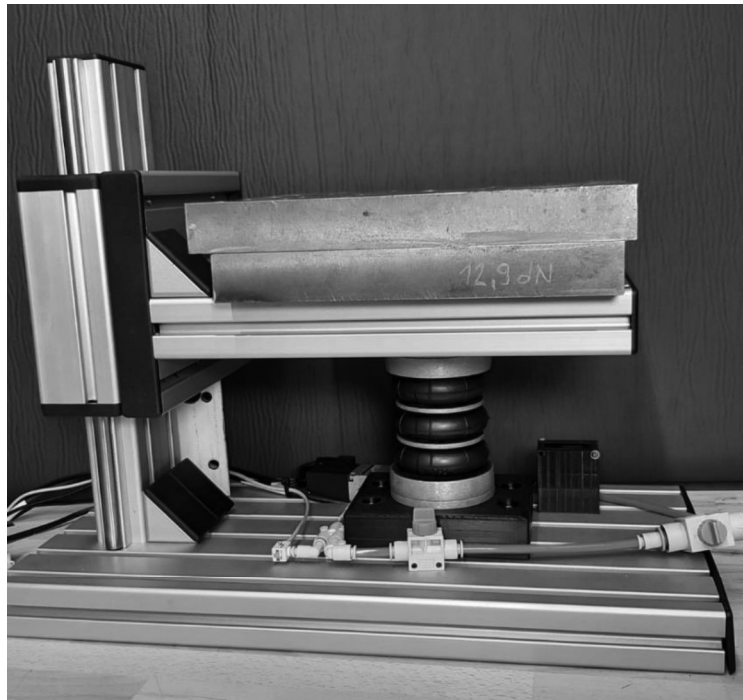


Figure 4: Assembled experimental device.

References

- [1] Rágulík, J.; Sivčák, M.: Modeling of the Controlled Air Spring, *Strojnícky časopis – Journal of Mechanical Engineering*, Vol. 69 (2019) No.3, pp. 107-112
- [2] Lillicrap, T.; Hunt, J; Pritzel, A.; Heess, N.; Erez, T.; Tassa, Y.; Silver, D.; Wierstra, D. (2015). Continuous control with deep reinforcement learning. CoRR.
- [3] Rágulík, J.; Sivčák, M.: Air springs controlled by reinforcement learning algorithm, *Proceedings of Engineering Mechanics 2020*, Fuis, V. (Ed.), pp. 428-431, ISBN 978-80-214-5896-3, Svratka, January 2020, Brno University of Technology, Brno, (2020)
- [4] Sutton, R.; Barto, A.: *Reinforcement Learning: An Introduction*, MIT Press, 2004
- [5] Visconti, P.; Giannotta, G.; Brama, R.; Primiceri, P.; Malvasi, A.; Centuori, A.: *Features, operation principle and limits of spi and I2C communication protocols for smart objects: A novel spi-based hybrid protocol especially suitable for IoT applications.*, *International Journal on Smart Sensing and Intelligent Systems*, Vol. 10 (2017) No.3, pp. 262-295

ON THE DEVELOPMENT OF THE SOFTWARE FOR TILTING-PAD JOURNAL BEARING DYNAMICS

Jan Rendl¹

Abstract: This contribution presents a computational model of tilting-pad journal bearings, which provide high stability of rotating machines and low sensitivity to load direction due to the pads' self-balancing. A robust nonlinear model of tilting-pad journal bearing was developed and employed in in-house software. The computational model considers hydrodynamic lubrication, out-of-balance forces, flexible support of the pads and potential Hertzian contacts between the journal and the pad.

1. Introduction

The paper focuses on the general mathematical model development of the tilting-pad journal bearing (TPJB) based on the decomposition of the system to the number of partial-arc journal bearings in the moving coordinate systems. Developed software for TPJB dynamics was fully implemented in MATLAB. Software is divided into two main parts. The first module is used for the modelling of fluid-structure interaction, which is represented by hydrodynamic force from squeezed oil film between the journal and each pad. The second module focuses on modelling individual pad motion and performing an investigation of rotor system behaviour in the time domain. The pads are described by lumped parameters.

The paper is outlined as follows. Section 2 is dedicated to a mathematical model of tilting-pad journal bearing. Section 3 contains the results of software verification and analysis of the dynamic behaviour of chosen TPJB systems. Finally, highlighted notes are concluded at the end of the paper.

2. Mathematical modelling of tilting-pad journal bearing

A scheme of considered system of the TPJB is depicted in Fig. 1. Journal centre position $S_J = [y_J(t), z_J(t)]$ is defined in the fixed Cartesian coordinate system yz . Rotational motion $\delta_i(t)$ of the pad about pivot point P_i is described in the auxiliary coordinate system $\xi_i\eta_i$. Each pad has its own local coordinate system $y'_i z'_i$, which is used for the formulation of governing equations of hydrodynamic lubrication.

Equations of motion of the rigid rotor with the mass $2m_J$ symmetrically supported by two identical TPJB can be written in the following form

$$\begin{bmatrix} m_J & 0 & 0 \\ 0 & m_J & 0 \\ 0 & 0 & I_{P,i} \end{bmatrix} \begin{bmatrix} \ddot{y}_J \\ \ddot{z}_J \\ \ddot{\delta}_i \end{bmatrix} = \begin{bmatrix} -m_J g + (\Delta m E) \omega^2 \cos(\omega t) + \sum_{i=1}^N F_{hd,i}^y \\ (\Delta m E) \omega^2 \sin(\omega t) + \sum_{i=1}^N F_{hd,i}^z \\ -m_{s,i} g [C_{\xi,i} \sin \phi - C_{\eta,i} \cos \phi] - F_{hd,i}^{y'} (R + \kappa_i) \end{bmatrix}. \quad (1)$$

The third equation has to be formulated for each pad and substitution $\phi(t) = \nu_i - \delta_i(t)$ is used for clarity of system of equations. Angle ν_i is the attitude angle to the i -th pivot in the fixed

¹ Ing. Jan Rendl; Faculty of Applied Sciences, University of West Bohemia, Technická 8, 301 00 Plzeň, Czech Republic, rendlj@ntis.zcu.cz

$$\begin{bmatrix} F_{cf,i}^{y'} \\ F_{cf,i}^{z'} \end{bmatrix} = -k_c |\Delta_{pen,i}|^{n_c} \begin{bmatrix} \sin \varphi_i \\ \cos \varphi_i \end{bmatrix}, \quad (4)$$

where k_c is the contact stiffness and n_c is the force exponent, $\Delta_{pen,i}$ is the penetration depth and φ_i is the attitude angle to the place where contact occurs. It is supposed it happens close to leading or trailing edges.

3. Results

A simple rigid rotor model supported by two TPJBs with four pads in load-between pad configuration was chosen for analysis. Parameters of TPJB were adopted from [1] and [3].

The software was firstly verified by comparing journal static equilibrium points presented in [3]. Figure 2 shows nominal values of vertical displacements and absolute errors between the results. The absolute errors are almost negligible in both analysed verification cases (Ver. 1 – zero preload and Ver. 2 – preloaded set-up). Figure 2 also contains calculated tilting angles of individual pads. It is obvious from the attached results that preloaded set-up strengthens the interaction between the journal and pad 1, which is almost unloaded in a non-preloaded set-up.

Adopted bearing from [1] was further analysed. The steady-state response to out-of-balance excitation was investigated. Obtained results are depicted in the form of bifurcation diagrams in Fig. 3. Each subfigure consists of static equilibrium points (yellow line) and local extremes distinguished by colour – maxima (red) and minima (black). There are interesting results for upper pads 1 and 2 where different nature of dynamic behaviour are apparent. Increasing rotor vibrations at 4000 rpm induce significant rotational motion of pad 1 with chaotic nature almost in whole speed range due to elastic contact at the leading edge. Lightly-loaded pad 2 has qualitatively different behaviour and the response developed from periodic motion and period-doubling to the chaotic nature.

5. Conclusion

Developed in-house software for complex analysis of the rotating system supported on tilting-pad journal bearing was introduced in this paper. A robust mathematical model was implemented in MATLAB. The software can analyse each pad's dynamic behaviour, solve fluid-structure interaction, and predict potential elastic contact between the journal and the pad. Particular results were verified by several published results and developed software for TPJB dynamics can be considered as reliable.

This work was supported by project SGS-2019-009.

References

- [1] Haugaard, A. M., and Santos, I. F.: Stability of multi orifice active tilting-pad journal bearings. *Tribology International*, Vol. 43(9), pp. 1742 – 1750.
- [2] Hori, Y. *Hydrodynamic Lubrication*. Springer-Verlag, Tokyo, ISBN 978-4-431-27898-6, (2006).
- [3] Someya T., *Journal-Bearing Databook*, Springer-Verlag, ISBN 3-570-17074-X, Berlin, (1989).

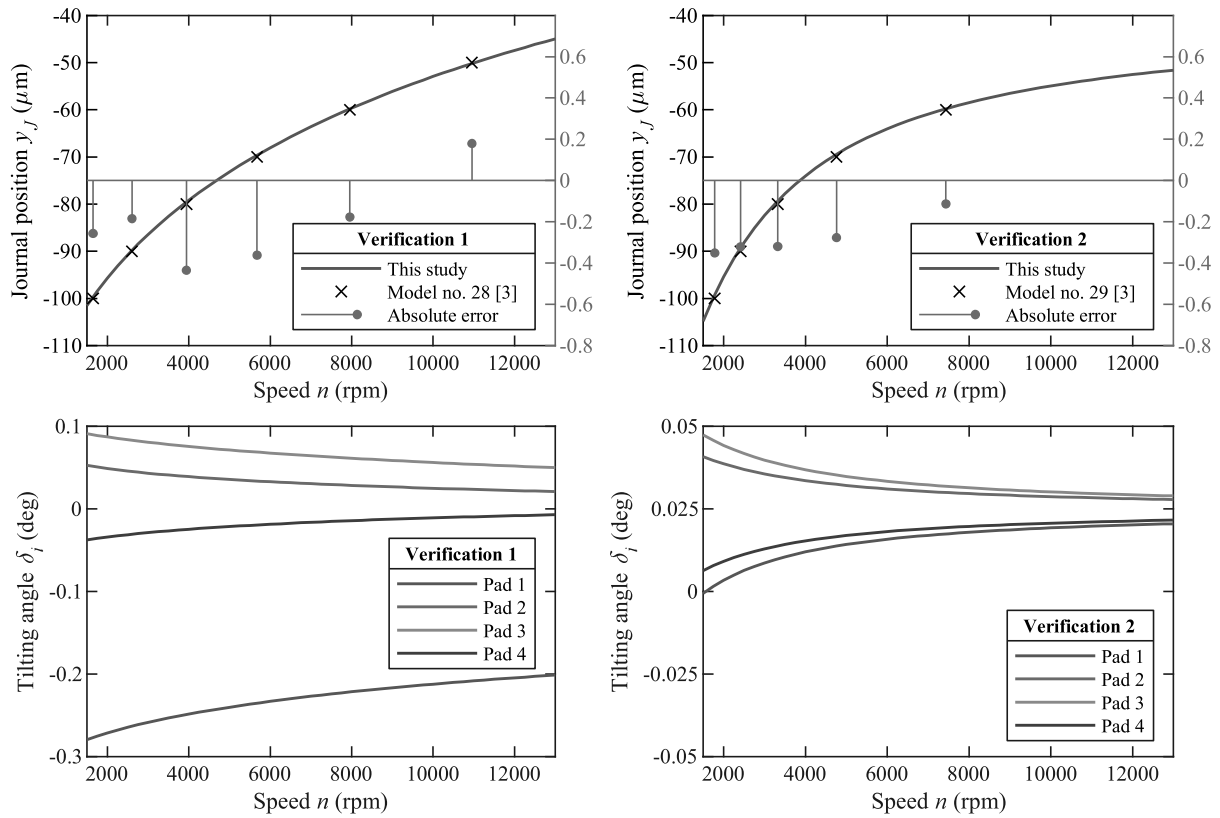


Figure 2: Static equilibrium points – verification of software with [3]

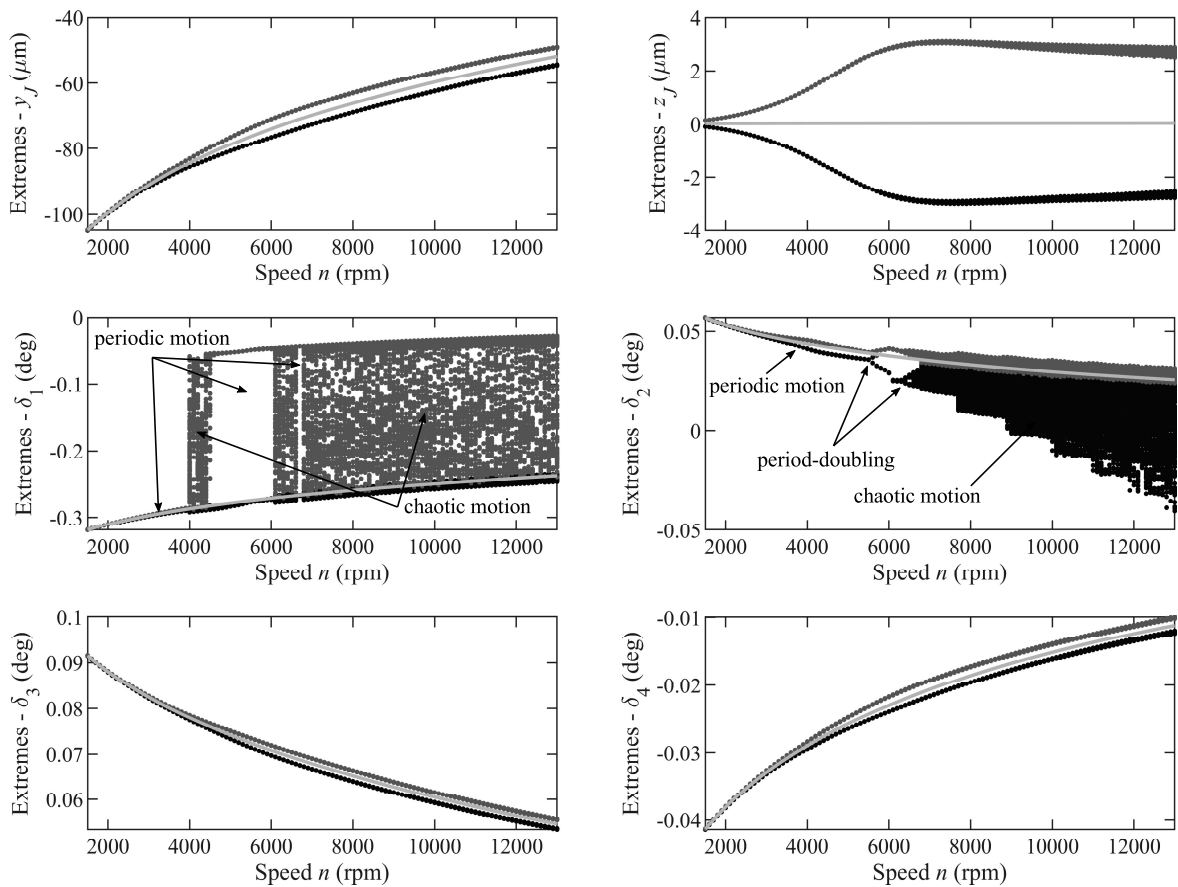


Figure 3: Bifurcation diagram and static equilibrium points of studied TPJB [1]

ELECTRIC POWER DISTRIBUTION SYSTEMS

Radek Skácelík¹

Abstract: Additive manufacturing (AM) processes, such as Selective Laser melting (SLM), have enabled the fabrication of geometrically complicated designs. However, undesired distortions due to thermally-induced residual stresses may lead to failure of the part. One of potential failure is a collision between recoater and printed part. In this paper, we address distortions and part failures due to collision and residual stress by using a finite element model to predict part distortion and gap under recoater.

1. Introduction

Additive manufacturing (AM) enables the fabrication of a three-dimensional object by depositing successive layers of material one on top of the other. Selective laser melting (SLM) build object from a metal powder by the laser beam power which melt powder at the object. This technology give freedom for object shape design, that makes SLM extremely attractive for deployment in a variety of unique environments, such as aircraft carriers or space vehicles.

2. Technologi SLM

Process of printing started with first layer of the powder. which is pull out from cartridge and pushed true printing area by recoater blade. Powder in the area is melted by laser beam, that's make one layer of the printed object (Fig. 2). Laser following pater (Fig. 1) which is changed every layer by rotation for elimination porosity. During the printing process, thermal stresses develop due to temperature gradients generated by the laser scanning pattern. Such stresses can result in macro-scale deformations and reduced strength, which often lead to loss of tolerance or even complete failure to print the part due to collision with recoater.

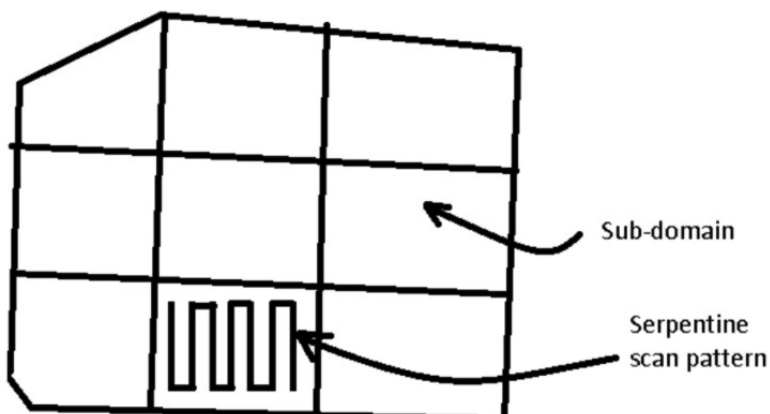


Figure 1: Laser scan pattern

¹ Ing. Radek Skácelík Czech Technical University in Prague, Department of mechanical Engineering; radek.skacelik@fs.cvut.cz

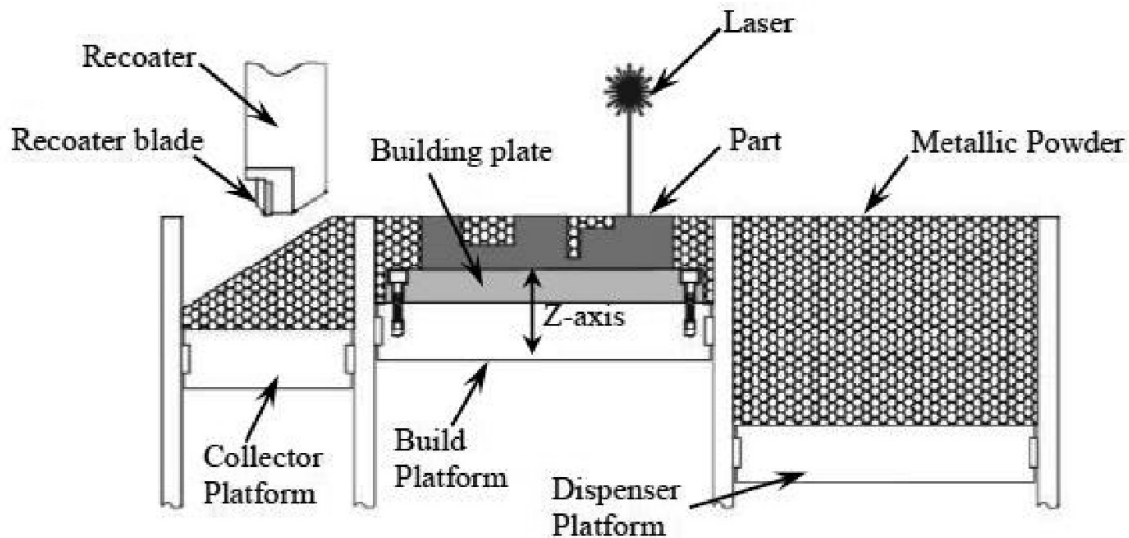


Figure 2: Schematic diagram of SLM fabricating equipment.[3]

Object is held on platform during support structures, after printing must by object undercut from platform and support structure remove from object. That is very slow and hand-operate process. Object orientation can reduce support structure on minimum, but object and support structure must be strong for thermal distortion and residual stress. Deformation can make collision with recoater.

Tisk a strategie tisku Kolize a chyby

3. Methodology

For the thermomechanical modeling of the SLM process, we utilize an uncoupled thermal and mechanical analyses. This means we first obtain the thermal results to later use them as initial conditions in the mechanical analysis. For computation is used adaptive domain reduction which divides the problem in two parts. First part is computed by explicit and second by implicit integration scheme [2]. This strategy uses explicit integration in domain when laser scan strategy produces temperature gradient. That is effective for time cost, because new material is added with small time increment. Every layer is represented by small elements of domain. When temperature field without influence of the heat produced by a laser is cooling down, is more effective exploit a long-time step increment from implicit integration with reduced number of elements. Interaction between domains used algorithms which has base in subcycling method.

3.1 Boundary conditions

Material undergoes complex processes, such as thermal conduction, heat loss due to convection and radiation, phase transformation, and melting and cooling solidification . Laser heat input is represented by Gaussian distribution of heat source (1) for simulate the interaction between the laser and materiál [1].

$$q(x, y, z) = \frac{3c_sQA}{\pi H(1 - \frac{1}{e^3})} \exp\left[\frac{-3c_s}{\log\left(\frac{H}{z}\right)}(x^2 + y^2)\right] \quad (1)$$

Where A is the laser absorptivity of materials affected by the wavelength, Q is the laser power, H is the height of heat source and C_s is the concentric coefficient of heat-flux distribution of the cross section. The enthalpy (H_e) is defined as a function of temperature (2). Where ρ is density and c is thermal capacity of based material

$$H_e = \int \rho c dT \quad (2)$$

The structural analysis assumes a small strain and small deformation formulation using an elasto-plastic constitutive model with the standard relation. The residual stress is formed after the cooling solidification stage. If the residual stress is greater than the yield strength of the material, it will produce local deformation. The material strain rate ε̇ is influenced by external force and temperature including the elastic strain rate ε_e, plastic strain rate ε_p, creep strain rate ε_c, and the strain rate caused by temperature change ε_T.

$$\epsilon = \epsilon_e + \epsilon_p + \epsilon_c + \epsilon_T \quad (3)$$

3.2 Deformation and colision of the object

Different of part volume can make heated areas when temperature depress slowly. This area we must put on same cooling gradient as other zone in the part. Temperature gradient is bigger at zone when heat went out true the part. Powder has less conductivity coefficient. Residual temperature close gap under recoater, prediction must compute structure distortion. Simulation used couple multi-physics thermal and structure mechanic. That is useful in preparing support structure

Experiments show the recoater risk is not only on thermal distortion but about object stiffness in recoater blade direction, for evaluation of stiffness was modal analysis as criterion for stiffness. Modal analysis is the study of the dynamic properties of systems in the frequency domain. That uses the overall mass and stiffness of a structure to find the various periods at which it will naturally resonate. When first frequency corresponds with lower stiffness zone in part. Modal analyses based on finale element simulation used computing roosts of stiffness matrix.

Simulation used mesh with deactivated elements. These elements are hidden in stiffness matrix. During computation is matrix of stiffness updated when is new layer added. It is powerful solution for first evaluation of oriented part stiffness in recoater side.

4. Experiment

Validation this method must separate thermal problem and stiffness. Printing machine EOS M290 printed cylinder with constant diameter. Thermal simulation and thermal camera optimized diameter for printing with rapid cooling down. That was granted test only for frequency minimum stiffness. Recoater impact print parts in specific layer and we compare with frequency. Recoater impact every part on platform and we find critical stiffness frequenci.

FUNDING

This research was funded from SGS program SGS21/150/OHK2/3T/12

References

- [1] CHENG, Bo, Subin SHRESTHA a Y. Kevin CHOU. Stress and Deformation Evaluations of Scanning Strategy Effect in Selective Laser Melting. In: *Volume 3: Joint MSEC-NAMRC Symposia* [online]. ASME, 2016, 2016-6-27, V003T08A009- [cit. 2019-06-06]. DOI: 10.1115/MSEC2016-8819. ISBN 978-0-7918-4991-0. Dostupné z: <http://proceedings.asmedigitalcollection.asme.org/proceeding.aspx?doi=10.1115/MSEC2016-8819>
- [2] KOEPF, J.A., D. SOLDNER, M. RAMSPERGER, J. MERGHEIM, M. MARKL a C. KÖRNER. Numerical microstructure prediction by a coupled finite element cellular automaton model for selective electron beam melting. *Computational Materials Science* [online]. 2019, **162**, 148-155 [cit. 2021-04-21]. ISSN 09270256. Dostupné z: [doi:10.1016/j.commatsci.2019.03.004](https://doi.org/10.1016/j.commatsci.2019.03.004)
- [3] LIU, Yang, Yongqiang YANG a Di WANG. A study on the residual stress during selective laser melting (SLM) of metallic powder. *The International Journal of Advanced Manufacturing Technology* [online]. 2016, **87**(1-4), 647-656 [cit. 2021-04-21]. ISSN 0268-3768. Dostupné z: [doi:10.1007/s00170-016-8466-y](https://doi.org/10.1007/s00170-016-8466-y)

AN ANALYSIS OF THE MECHANICAL PROPERTIES OF POROUS CERAMIC FOAMS FOR BONE SUBSTITUTES DURING ACCELERATED DEGRADATION

Martin Vltavský¹, Radek Sedláček¹, Tomáš Suchý¹

Abstract: The aim of this work was to analyze the mechanical properties of porous ceramic foams for bone tissue replacement during accelerated degradation. An experiment was performed, consisting of a compression test of calcium phosphate samples exposed to the medium mimicking the osteoclastic degradation for 10 min, 4 h and 8 h. Then the weight loss was determined, a microscopic analysis was performed, and the free calcium ion release and the pH of the medium were determined. The ultimate strength in compression was the evaluated mechanical properties parameter. The statistical significance of the detected differences was analyzed by applying standard statistical procedures.

1. Introduction

With the growing working population has increased a possibility of bone fractures and defects, which are considered as the most frequent cause of disability. Among the most important complications related to the treatment of bone traumas belong infections during the healing period. Once is a bone defect filled with hematoma or fibrous tissue, it often becomes a breeding ground for bacteria and leads to the development of osteomyelitis. Moreover, insufficient cortical bone volume, when placing implants can lead to lack of primary stability, which could threaten the osseointegration process [1],[2].

Currently, one of the acknowledged methods for managing infected total hip or knee arthroplasties are one- or the-stage revisions. Among the most used materials in two-stage revision belongs poly(methyl methacrylate) (PMMA) loaded with antibiotics [3]. Although these bone cement spacers have been considered the gold standard for such applications, it is associated with undesired disadvantages, such as high hardening temperature, limited porosity or insignificant degradation [4]. Thus, with a view to overcoming the mentioned drawbacks, a high emphasis is placed on the development of novel replacement systems based on composite advanced materials.

More recently, bone tissue engineering has provided many synthetic alternatives among them calcium phosphate cements (CPC) entice substantive attention. These materials are bioactive, resorbable and injectable, making them very attractive in minimally invasive surgery [5]. Although they evince excellent biological behavior, it is being reported, that they have poor mechanical properties limiting their application mainly to non-loadbearing or moderately loadbearing situations [6].

The aim of this study was to investigate the ultimate compression strength, the elastic gradient, the absorbed energy, the work of fracture and the structural changes that occur during the biodegradation of 6 different kinds of CPC scaffolds with a similar macrostructure but with different fabrication and composition. In an attempt to mimic the osteoclastic environment during bone remodeling, a degradation experiment was performed in an acidic medium of pH 2 [7]. Although there are publications on the degradation of CPC in vivo and in

¹ Ing. Martin Vltavský, Ing. Radek Sedláček, Ph.D., Ing. Tomáš Suchý, Ph.D.; Czech Technical University in Prague, Faculty of Mechanical Engineering, Department of Mechanics, Biomechanics and Mechatronics, Technická 4, 160 00 Praha 6, Czech Republic; Martin.Vltavsky@fs.cvut.cz, Radek.Sedlacek@fs.cvut.cz, Tomas.Suchy@fs.cvut.cz

vitro, they primarily describe only its kinetics. Its influence on the change of mechanical properties of

the scaffold is rarely published. However, for the proper function of the implant, it is necessary to monitor their properties not only in the dry state, but also in the conditions in which they will be subsequently implanted in the body. The final cement aims to eliminate possibilities of bone infection, actively stimulates bone tissue regeneration and enables minimally invasive application, resulting in decreased burden of surgical procedure on patient.

2. Methods and Materials

The aim of the methodology and the realization of the experiments was to make an analysis of mechanical properties. Six kinds of ceramic scaffolds were prepared that differed either by their fabrication or by the composition of the additives that were used. All samples consisted of a mixture of poly(lactic acid), poly(glycolic acid) and poly(ethylene glycol) (PLGA-PEG-PLGA) with alpha-tricalcium phosphate (α -TCP). The basic material is signed B. The exact sample composition and fabrication with the assigned abbreviation is shown in Table 1.

Table 1: Labeling, composition and fabrication of the samples

Abbreviation	Additives	Fabrication
B H	-	H
B S	-	E.S.
B+PCL H	PCL fibers	H
B+PCL S	PCL fibers	E.S.
B+A H	Amine	H
B+PCL+A S	PCL fibers + Amine	E.S.

Note: H – mixed by hand; E.S. – stirred by an electrical stirrer; PCL – Polycaprolactone

The accelerated degradation testing was conducted according to Escudero et al. [7]. The samples were immersed for 10 min, 4 hours and 8 hours in a solution consisting of 0.01 M HCl and 0.14 M NaCl, with pH = 2.2 at 37°C. The solution was changed every hour, and the pH values were checked at each time-point in the collected supernatants, using an IKATRON THETA 90 electrode (IKA Werke, Staufen im Breisgau, Germany). The calcium concentration of the solution was measured at each time-point using an HI4104 calcium ion selective electrode (HANNA Instruments, GmbH, Austria).

The methodology for compression testing the samples was performed according to the ISO 13 314 standard [8]. The measurements were carried out at a constant initial speed of 3.6 mm.min⁻¹ (deformation rate in the range of 10⁻² - 10⁻³ s⁻¹). The statistical significance was analyzed using STATGRAPHICS Centurion XV (Statpoint, USA). The median values were calculated for the number of readings (n) from each experiment; the error bars refer to the interquartile range (IQR). Statistical significance was accepted when $p \leq 0.05$.

In addition to the compressive testing, the experiment was supplemented by an image analysis of the scanning electron microscopy (SEM) images made on a Quanta 450 electron microscope (FEI, USA). In order to ensure good resolution, the samples were coated with a thin layer of carbon (Emitech K550X, Quorum Technologies, UK). The same specimens which were analyzed via SEM were scanned using micro-CT SkyScan 1272 (Bruker micro-CT, Kontich, Belgium). Scaffold structure analysis, including porosity analysis, was performed by means of a CTAn (Bruker).

3. Results

The morphological changes in the microstructure of a scaffold during degradation are depicted in Figure 1. The scaffolds before degradation (top row) show a typical crystal-entangled cement microstructure with the plate-like character of precipitated calcium-deficient hydroxyapatite (CDHA) crystals. After 4 hours of degradation, some spherical pores were formed on the surface of the scaffold. A more detailed observation at higher magnification revealed the disappearance of the plate-like crystal microstructure as a consequence of the dissolution the CDHA crystals. Figure 2 shows inner 3D structure of the scaffold B+PCL+A S taken by micro-CT. All materials exhibited open and closed porosity, which support generation interconnected pores. The high interconnectivity of porous scaffolds with macropores interconnected by micropores enhanced biocompatibility and biodegradability.

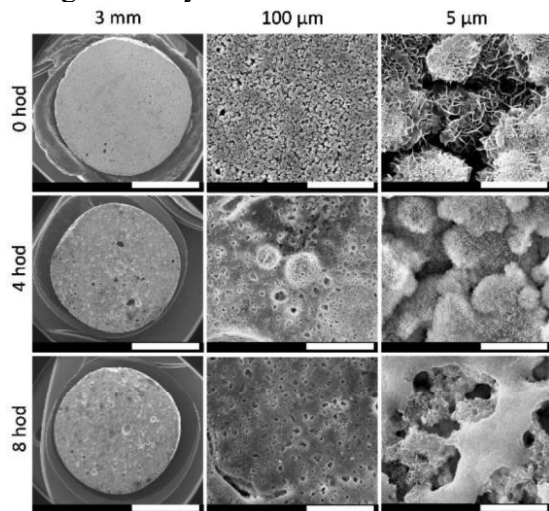


Figure 1: SEM images of the microstructure of the B+PCL+A S after 0, 2 and 8 h of accelerated degradation with a scale bar of 3mm (left), 100 μm (centre) and 5 μm (right)

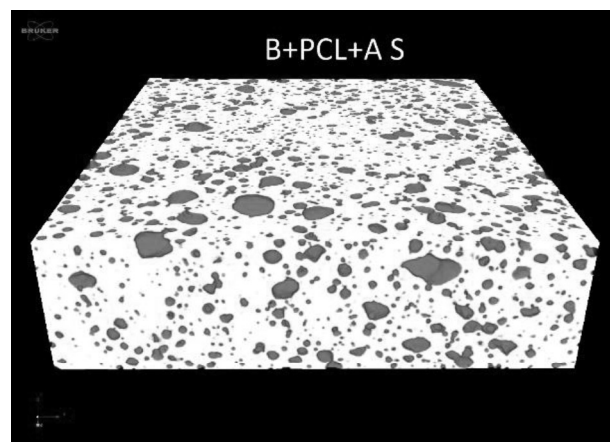


Figure 2: micro-CT image of inner 3D structure of the scaffold B+PCL+A S

The accelerated degradation test presented here was based on an acidic milieu attaining values of below pH 3 generated by osteoclasts in the bone resorption process and resulting in the dissolution of underlying minerals that showed itself in the form of the release free calcium Ca^{2+} ions. The acidic solution employed in the experiment sustained the pH in the range of about 2 – 2.2. The volume of medium used can therefore be considered sufficient from the point of view of maintaining a stable pH level.

the concentration values range between 0.9 - 1.1 mmol.l^{-1} . An acidic environment simulating osteoclast activity caused CDHA to dissolve, as seen in the SEM image, which led to the release of calcium Ca^{2+} ions into the solution. This could indicate that the remodeling process is set up, but further experiments would be needed to confirm this assumption. Cement degradation could be too rapid for bone to reach the material. Too rapid degradation could lead to fibrous encapsulation, which is an undesirable effect

The following graph (see Figure 3) shows the degradation development of the mass loss in the medium within one material. After statistical analysis, it is clear from the graph that due to exposure, the weight loss increases significantly after eight hours for all tested materials. After eight hours, an increase in the value of weight loss of about 60% was recorded for all materials. When comparing the mass loss values in the individual exposure states, no statistically significant differences were found between the materials in any of the exposure states.

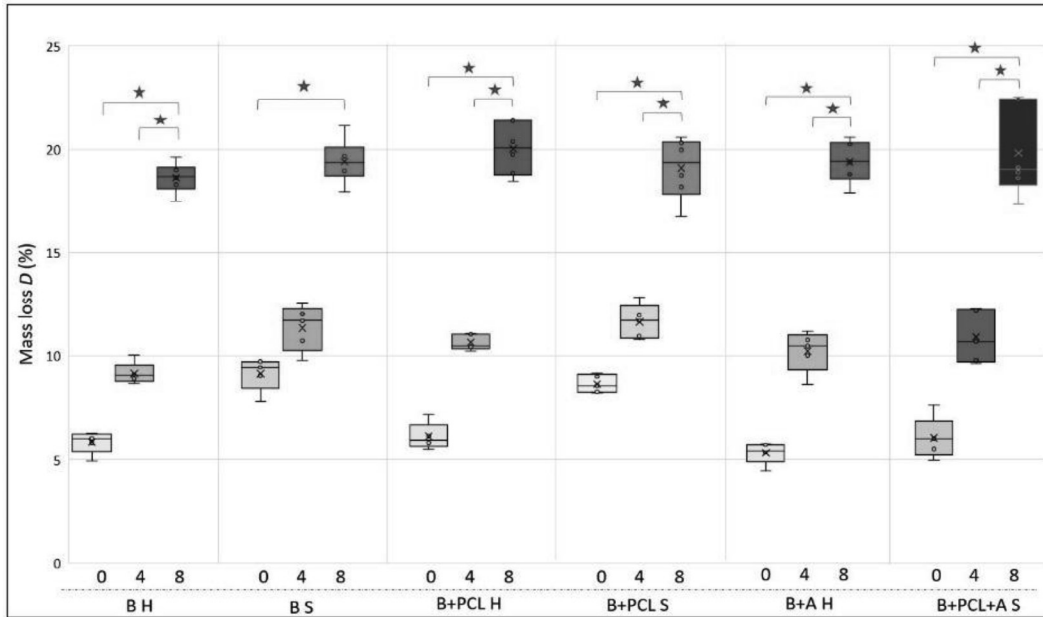


Figure 3: Graphical comparison of calculated values of weight loss within one material (type 2); * indicates a statistically significant difference (for PA + AM: M-W, $p < 0.01667$; for others: LSD test, $p < 0.05$, $n = 6$)

In the following section will be displayed only results from analysis of ultimate compressive strength. Figure 4 shows the ultimate compressive strength before and after 4 and 8 hours of exposure in the medium. It shows that the ultimate compressive strength of all tested samples decreased with the exposure time in the medium, probably as a consequence of the dissolution of the CDHA crystals. The range of compressive strength was in good agreement with the strength of trabecular bone (0.6-15 MPa) [9]. Moreover, the influence of the fabrication of the scaffolds is clear. The samples that were stirred by the electrical stirrer reached lower compressive strength values than those that were stirred manually. Another finding that can be observed from the graph in Figure 4 is the influence of the PCL fibers. The statistical analysis showed no statistically significant differences between samples with or without PCL fiber.

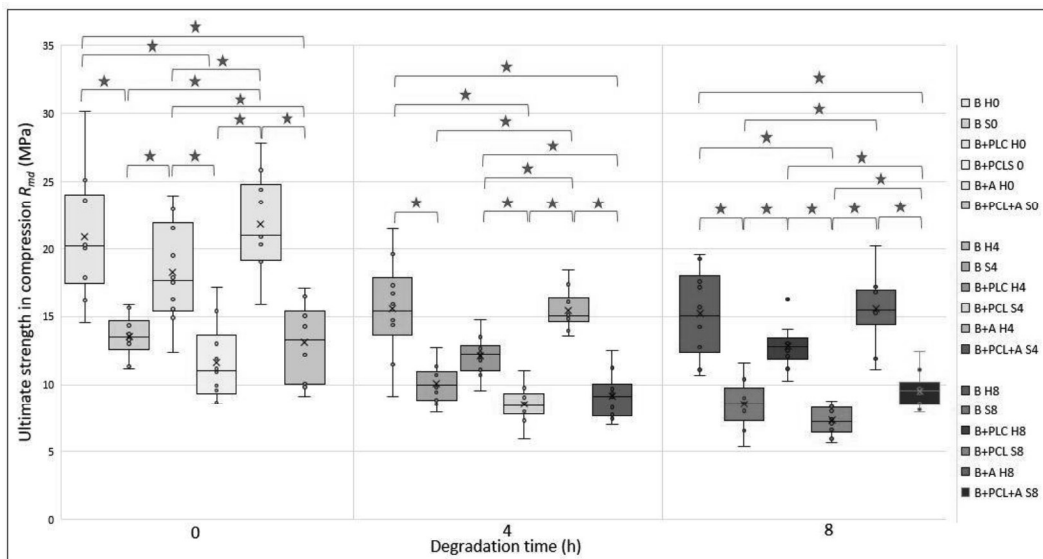


Figure 4: Graphical comparison of calculated values of ultimate strength in compression between materials (type 1); * indicates a statistically significant difference when comparing the material at each exposure time separately (for 0 hours: LSD, $p < 0.05$; for 4.8 hours: M-W, $p < 0.008334$, $n = 10$)

4. Conclusions

The accelerated degradation test presented here was based on an acidic milieu attaining values of below pH 3 generated by osteoclasts in the bone resorption process and resulting in the dissolution of underlying minerals. The dissolution showed itself in the form of the release free calcium Ca^{2+} ions. Although the used in vitro model of the medium does not capture the complexity of the degradation that occurs in the body, this study does demonstrate changes in mechanical properties, the topographic changes of materials surface, the structural changes in internal material architecture, the mass loss of the cement and the release of calcium ions over the exposure time. Based on these findings, it can be assumed that there is a gradual degradation of the material in the tested cements.

We found that the stirring with an electrical stirrer leads to lower ultimate compressive strength. We assume that air bubbles were introduced into the materials during mixing, and that this increased the porosity of the material. This led to a reduction in compressive strength.

These experiments also revealed the advantage of applying PCL fibers. The addition of PCL fibers to the mixture did not significantly improve or deteriorate the mechanical properties. We therefore came to the conclusion that these fibers could be used as a drug delivery system. According to the achieved results, stirred foams with derived amin and PCL fibers appears to be the ideal combination of the tested materials for bone replacements due to sufficient mechanical properties, which correspond to currently used bone cements as well as to spongy bone, satisfactory structural properties and compared to other tested materials improved biological properties

Acknowledgements

This study was supported by the Ministry of Health of the Czech Republic under grant NV18-05-00379.

References

- [1] WANG, Wenhao a Kelvin W. K. YEUNG. Bone grafts and biomaterials substitutes for bone defect repair: A review [online]. *Bioactive materials*. 2017, 2(4), 224-247. Dostupné z: 10.1016/j.bioactmat.2017.05.007.
- [2] LEW, Daniel P. a Francis A. WALDVOGEL. Osteomyelitis [online]. *The Lancet*. 2004, 364(9431), 369-379. Dostupné z: 10.1016/S0140-6736(04)16727-5.
- [3] SHI, Meng, James D. KRETLOW, Anson NGUYEN, Simon YOUNG, L. SCOTT BAGGETT, Mark E. WONG, F. Kurtis KASPER a Antonios G. MIKOS. Antibiotic-releasing porous polymethylmethacrylate constructs for osseous space maintenance and infection control [online]. *Biomaterials*. 2010, 31(14), 4146-4156. Dostupné z: 10.1016/j.biomaterials.2010.01.112.
- [4] LAREDO, Jean-Denis a Bassam HAMZE. Complications of percutaneous vertebroplasty and their prevention [online]. *Seminars in Ultrasound, CT and MRI*. 2005, 26(2), 65-80. Dostupné z: 10.1053/j.sult.2005.02.003.
- [5] FERNANDEZ DE GRADO, G., L. KELLER, Y. IDOUX-GILLET, Q. WAGNER, A. MUSSET, N. BENKIRANE-JESSEL, F. BORNERT and D. OFFNER. Bone substitutes: a review of their characteristics, clinical use, and perspectives for large bone defects management. *Journal of Tissue Engineering*. 2018, 9. DOI: 10.1177/2041731418776819. ISSN 2041-7314.
- [6] ZHANG, J., W. LIU, V. SCHNITZLER, F. TANCRET and J. BOULER. Calcium phosphate cements for bone substitution: Chemistry, handling and mechanical properties. *Acta Biomaterialia*. 2014, 10(3), 1035-1049, DOI: 10.1016/j.actbio.2013.11.001. ISSN 17427061.

[7] DIEZ-ESCUADERO, A., M. ESPANOL, S. BEATS and M.-P. GINEBRA. In vitro degradation of calcium phosphates: Effect of multiscale porosity, textural properties and composition. *Acta Biomaterialia*. **2017**(60), 81-92

[8] ČSN ISO 13314. *Mechanické zkoušení kovů - Zkoušení tvářitelnosti - Zkouška porézních a pěnových kovů tlakem*. Praha: Úřad pro technickou normalizaci, metrologii a státní zkušebnictví. 2012, 12 s. Třídící znak 42 0439.

[9] CARTE, D.; HAYES, W. The compressive behavior of bone as a two-phase porous structure. *J. Bone Jt. Surg. Ser. A* **1977**, 59, 954–962.



APPLIED MECHANICS 2021

Liberec, 22nd April - 23th April

TECHNICAL UNIVERSITY OF LIBEREC, FACULTY OF MECHANICAL ENGINEERING
STUDENTSKÁ 1402/2, 461 17 LIBEREC, CZECH REPUBLIC

